Biophysical Journal
Article

Biophysical Society

Rate-Dependent Role of I_{Kur} in Human Atrial Repolarization and Atrial Fibrillation Maintenance

Martin Aguilar,[1,2] Jianlin Feng,[3] Edward Vigmond,[4,5] Philippe Comtois,[1,2] and Stanley Nattel[1,6,7,8,9,*]

[1]Research Center, Montreal Heart Institute and [2]Department of Pharmacology and Physiology/Institute of Biomedical Engineering, Université de Montréal, Montreal, Québec, Canada; [3]Bristol-Myers Squibb, Wallingford, Connecticut; [4]L'Institut de Rythmologie et Modélisation Cardiaque LIRYC, Fondation Université de Bordeaux, Hôpital Xavier-Arnozan, Pessac, France; [5]Institut de Mathématiques de Bordeaux, Université de Bordeaux, Talence, France; [6]Department of Medicine and [7]Department of Pharmacology and Therapeutics, McGill University, Montreal, Québec, Canada; [8]Department of Medicine, Université de Montréal, Montreal, Québec, Canada; and [9]West German Heart and Vascular Center, Faculty of Medicine, University Duisburg-Essen, Essen, Germany

ABSTRACT The atrial-specific ultrarapid delayed rectifier K^+ current (I_{Kur}) inactivates slowly but completely at depolarized voltages. The consequences for I_{Kur} rate-dependence have not been analyzed in detail and currently available mathematical action-potential (AP) models do not take into account experimentally observed I_{Kur} inactivation dynamics. Here, we developed an updated formulation of I_{Kur} inactivation that accurately reproduces time-, voltage-, and frequency-dependent inactivation. We then modified the human atrial cardiomyocyte Courtemanche AP model to incorporate realistic I_{Kur} inactivation properties. Despite markedly different inactivation dynamics, there was no difference in AP parameters across a wide range of stimulation frequencies between the original and updated models. Using the updated model, we showed that, under physiological stimulation conditions, I_{Kur} does not inactivate significantly even at high atrial rates because the transmembrane potential spends little time at voltages associated with inactivation. Thus, channel dynamics are determined principally by activation kinetics. I_{Kur} magnitude decreases at higher rates because of AP changes that reduce I_{Kur} activation. Nevertheless, the relative contribution of I_{Kur} to AP repolarization increases at higher frequencies because of reduced activation of the rapid delayed-rectifier current I_{Kr}. Consequently, I_{Kur} block produces dose-dependent termination of simulated atrial fibrillation (AF) in the absence of AF-induced electrical remodeling. The inclusion of AF-related ionic remodeling stabilizes simulated AF and greatly reduces the predicted antiarrhythmic efficacy of I_{Kur} block. Our results explain a range of experimental observations, including recently reported positive rate-dependent I_{Kur}-blocking effects on human atrial APs, and provide insights relevant to the potential value of I_{Kur} as an antiarrhythmic target for the treatment of AF.

INTRODUCTION

The ultrarapid delayed rectifier K^+ current (I_{Kur}) was originally described as a rapidly activating, 4-aminopyridine-sensitive K^+ current with slow and limited inactivation (1). However, many of the original experiments used relatively short test pulses, typically <4 s long, which may have not been enough to observe the full extent of I_{Kur}'s inactivation. Feng et al. (2), using longer 50-s test pulses, showed that I_{Kur} inactivates almost completely when the cell is depolarized to +40 mV, with a biexponential time course comprising fast (τ_f) and slow time constants (τ_s) of 1.0 and 6.8 s, respectively. Based on these experiments, it has been hypothesized that I_{Kur} inactivation may play an important role under physiological conditions, specifically related to I_{Kur} frequency-dependent dynamics (2). The potential for full inactivation of I_{Kur} suggests that the contribution of the current would decrease at faster rates, as the total amount of time when the cell is depolarized increases and inactivation accumulates. However, recent experimental results using the I_{Kur}-selective blocker XEN-D0103 suggest the opposite, and indicate that the contribution of I_{Kur} to atrial repolarization increases at higher rates (3).

To our knowledge, none of the commonly used mathematical models of the human atrial cardiomyocyte action potential (AP) integrate the experimentally defined I_{Kur} inactivation dynamics reported by Feng et al. (2). To better understand the rate-dependent role of I_{Kur} and the effect of blocking it on the human atrial AP, it is necessary to use a model with accurate inactivation properties. In this study, we sought to 1) quantify the kinetic features of the I_{Kur}

Submitted November 21, 2016, and accepted for publication March 23, 2017.

*Correspondence: stanley.nattel@icm-mhi.org

Philippe Comtois and Stanley Nattel contributed equally to this work.

Editor: Eric Sobie.

http://dx.doi.org/10.1016/j.bpj.2017.03.022

inactivation properties defined by Feng et al. (2); 2) update the Courtemanche human atrial AP model (4) to include realistic I_{Kur} inactivation parameters; 3) investigate the rate-dependent properties of I_{Kur} inactivation over the course of the AP under physiological conditions; 4) evaluate the contribution of I_{Kur} with realistic inactivation properties to human atrial repolarization at different frequencies; and 5) evaluate the potential consequences for effects of blocking I_{Kur} on atrial fibrillation (AF) in non-remodeled and AF-remodeled atrial tissue.

MATERIALS AND METHODS

Mathematical modeling of I_{Kur} inactivation

The experimental data recorded by Feng et al. (2) were used as the basis for model development in our study. A description of the experimental methods can be found in the original article (2). The Courtemanche human atrial cardiomyocyte model was implemented (4). The original formulation of the I_{Kur} inactivation parameter is as follows:

$$I_{Kur} = C_m \times g_{Kur} \times u_a^3 \times u_i \times (V - E_K),$$

$$g_{Kur} = 0.005 + \frac{0.05}{1 + \exp\left(-\frac{V - 15}{13}\right)},$$

$$\alpha_{ui} = \left[21 + \exp\left(-\frac{V - 185}{28}\right)\right]^{-1},$$

$$\beta_{ui} = \exp\left(\frac{V - 158}{16}\right),$$

$$\tau_{ui} = [\alpha_{ui} + \beta_{ui}]^{-1}/K_{Q10},$$

$$u_{i,\infty} = \left[1 + \exp\left(\frac{V - 99.45}{27.48}\right)\right]^{-1},$$

$$\frac{du_i}{dt} = \frac{u_{i,\infty} - u_i}{\tau_{ui}},$$

where I_{Kur} is the ultrarapid delayed rectifier K^+ current, g_{Kur} is the maximal I_{Kur} conductance, V is the transmembrane potential, E_K is the K^+ equilibrium potential, and u_a and u_i are I_{Kur}'s activation and inactivation gating variables, respectively; α_{ui} and β_{ui} are the forward and backward rate constants for the inactivation gate variable, respectively; τ_{ui} is the time constant; $u_{i,\infty}$ is the steady-state relation for the inactivation gate variable; C_m is the membrane capacitance (100 pF); and K_{Q10} is a scaling factor (3).

To account for I_{Kur} inactivation dynamics we replaced the original inactivation gating variable u_i by fast ($u_{i,f}$) and slow ($u_{i,s}$) inactivation gating variables. The gating variables and time constant parameters were fitted by iteratively minimizing the mean error of the model time constants relative to experimentally derived values obtained with a 50-s test-pulse at 0, 10, 20, 30, 40, and 50 mV (Fig. S1, *B* and *C*); the modified inactivation gating variables and time constants are given by the following:

$$\tau_{ui,f} = 800 \times \left(2 - \left[\frac{V}{40}\right]\right),$$

$$u_{i,f\infty} = \left[1 + \exp\left(\frac{V - 35}{20}\right)\right]^{-1},$$

$$\tau_{ui,s} = 5800 \times \left[1 + \exp\left(-\frac{V + 80}{11}\right)\right]^{-1},$$

$$u_{i,s\infty} = \left[1 + \exp\left(\frac{V + 5}{5}\right)\right]^{-1},$$

$$\frac{du_{i,x}}{dt} = \frac{u_{i,x\infty} - u_{i,x}}{\tau_{ui,x}},$$

$$I_{Kur} = C_m \times g_{Kur} \times u_a^3 \times u_{i,s} \times u_{i,f} \times (V - E_K).$$

The activation gating variable and time constant were not modified and are given by the following:

$$\tau_{ua} = [\alpha_{ua} + \beta_{ua}]^{-1}/K_{Q10},$$

$$\alpha_{ua} = 0.65\left[\exp\left(-\frac{V + 10}{8.5}\right) + \exp\left(-\frac{V - 30}{59}\right)\right]^{-1},$$

$$\beta_{ua} = 0.65\left[2.5 + \exp\left(\frac{V + 82}{17}\right)\right]^{-1},$$

$$\tau_{ua} = [\alpha_{ua} + \beta_{ua}]^{-1}/K_{Q10},$$

$$u_{a,\infty} = \left[1 + \exp\left(-\frac{V + 30.3}{9.6}\right)\right]^{-1}.$$

The activation gate open probability is given by u_a^3. The inactivation gate open probability in the original model was given by u_i; in the modified model $u_{i,s} \times u_{i,f}$ was used to reflect the combined effects of slow and fast inactivation components. Open probabilities range from 0 (closed) to 1 (open). The charge carried by I_{Kur} in one cardiac cycle, given by the area under the I_{Kur}-versus-time curve (Kur AUC), was calculated by integrating I_{Kur} over one cardiac cycle. The activation gate open-probability area under the curve (u_a^3 AUC) was calculated by integrating u_a^3 over one cardiac cycle. The AP amplitude was defined as the difference between the peak phase-0 overshoot potential and the resting membrane potential.

Mathematical simulations

The Courtemanche model of human atrial cardiomyocyte bioelectricity was implemented with the original and updated I_{Kur} inactivation formulations. The total ionic current for the model (I_{tot}) was given by the following:

$$I_{tot} = I_{Na} + I_{K1} + I_{to} + I_{Kur} + I_{Kr} + I_{Ks} + I_{Ca,L} + I_{p,Ca} + I_{NaK} + I_{NaCa} + I_{b,Na} + I_{b,Ca} + I_{K,ACh},$$

where I_{Na} is the fast inward Na^+ current; I_{K1} is the inward rectifier K^+ current; I_{to} is the transient outward K^+ current; I_{Kur}, I_{Kr}, and I_{Ks} are the ultrarapid, rapid, and slow components of the delayed rectifier K^+ current, respectively; $I_{Ca,L}$ is the L-type inward Ca^{2+} current; $I_{p,Ca}$ is the sarcolemmal Ca^{2+} pump current; I_{NaK} is the Na^+/K^+ pump current; I_{NaCa} is the Na^+/Ca^{2+} exchanger current; $I_{b,Na}$ is the background Na^+ current; $I_{b,Ca}$ is the background Ca^{2+} current; and $I_{K,ACh}$ is the acetylcholine-activated K^+ current (5). Isolated cardiomyocyte APs were simulated at 37°C by numerical integration with the software MATLAB's ODE23s ordinary differential equation solver (The MathWorks, Natick, MA) with a relative tolerance of 10^{-2}. For each condition, pacing was sustained for 280 cycles with 2-ms 3 nA stimuli and the last action potential was used for analysis.

Computer simulations of the effect of I_{Kur} block on AF were performed with the CARP simulator, which solves the monodomain equation by the finite element method as described previously (6), as follows:

$$\nabla \times \sigma_i \nabla V = \beta\left(C_m \frac{\partial V}{\partial t} + I_{tot}\right),$$

where σ_i is the tissue conductivity, β is the membrane surface-to-volume ratio (0.14 μm^{-1}), and C_m is the membrane capacitance (1 $\mu F/cm^2$). The updated Courtemanche ionic model was adapted and implemented in CARP. Conductivities were chosen to give a physiological conduction velocity in the longitudinal direction (47.9 cm/s). The tissue measured 7 × 6 cm with fibers oriented along the long dimension with an anisotropy ratio of ~6. The grid was discretized at 100-μm resolution and equations solved with a 25-μs timestep. Reentry was initiated by a standard S1-S2 cross-shock protocol with an S1-S2 interval of 170 ms.

Two-dimensional simulations were conducted using three different acetylcholine (ACh) distribution patterns (one homogeneous ACh distribution and two sinusoidal distributions) and three peak ACh concentrations (1.875, 3.75, and 7.5 nM), generating nine conditions. I_{Kur} block was simulated by a fixed reduction in maximal I_{Kur} conductance (g_{Kur}). Dose-response curves were generated by introducing I_{Kur} block at 10 different time-points {t_{drug} = 1000 ms, 1100 ms, … 1800 ms, 1900 ms} for each percent I_{Kur} block {10%, 20%, …, 90%, 100%}; the average time to termination was quantified as the time from t_{drug} to reentry termination. Simulations were run using the control (non-remodeled) Courtemanche human atrial AP model and repeated with an AF-remodeled AP model consisting of the control model with the following modifications: I_{to} conductance reduced by 50%, I_{Kur} conductance reduced by 50%, $I_{Ca,L}$ conductance reduced by 70%, and I_{K1} conductance increased by 100% (7).

RESULTS

Experimentally observed time-dependent inactivation of I_{Kur}

The ultrarapid delayed rectifier K^+ current (I_{Kur}) is often described as having slow and partial inactivation. Fig. 1 *A* shows normalized I_{Kur} during a 1000 ms test-pulse to +40 mV, 5 ms after a 100-ms pretest pulse to +40 mV to inactivate I_{to}, as recorded experimentally (*black*) (2) and from the original Courtemanche human atrial I_{Kur} formulation (*blue*). Using this relatively short test pulse, experimental I_{Kur} inactivates by ~45% (*black*). In contrast to experimental data, in the original Courtemanche model, I_{Kur} does not inactivate appreciably over the course of the pulse (*blue*). Fig. 1 *B* shows normalized I_{Kur} during a longer, 50 s test-pulse to +40 mV, 5 ms after a 100-ms pretest pulse to +40 mV to inactivate I_{to}. With the longer pulse, the experimentally recorded I_{Kur} (*black*) inactivated completely with a biexponential time-course characterized by fast and slow time constants of 702 ± 7 and 5688 ± 26 ms, respectively. Again, the original Courtemanche model (*blue*) fails to reproduce I_{Kur}'s inactivation dynamics, with 85% of the peak current persisting at the end of the 50-s test-pulse.

Model inactivation kinetics modified according to experimental data

To accurately reproduce the experimentally recorded I_{Kur} inactivation kinetics, we modified the Courtemanche model by introducing a set of slow ($u_{i,s}$) and fast ($u_{i,f}$) inactivation gating variables in place of the single inactivation gating variable (u_i) in the original model. The voltage dependence of the inactivation gating variables for the original ($u_{i,original}$, *blue line*) and modified ($u_{i,f}$, *red solid line*; $u_{i,s}$, *red dashed line*) models is shown in Fig. S1 *A*. The major modification to inactivation gating is more complete inactivation at depolarized potentials; the complete mathematical formulation can be found in Materials and Methods. We also replaced the inactivation time constant ($\tau_{ui,original}$) with a set of fast ($\tau_{ui,f}$) and slow ($\tau_{ui,s}$) inactivation time constants (Fig. S1 *B*). Note that the updated inactivation time constants are of the order of 1–6 s. The voltage dependence of the activation gating variable (Fig. S1 *C*; $u_{a,x}$) and activation time constant (Fig. S1 *D*, $\tau_{ua,x}$) were not modified. The activation time constant is in the range of 1–6 ms.

The modified model (*red line*) closely reproduced the experimentally recorded current inactivation (*black line*) during a prolonged pulse (Fig. 1 *B*) and the experimentally recorded I_{Kur} inactivation kinetics (Fig. 1 *C*) at 37°C. Excellent agreement between experiments and the mathematical model was obtained across the spectrum of test potentials.

Time-, voltage-, and frequency dependence of I_{Kur} inactivation

We then compared the time dependence of I_{Kur} inactivation in the model to experimental results obtained by varying the duration of the test pulse. Fig. 1 *D* (*black*) shows experimentally recorded normalized I_{Kur} obtained with conditioning pulses to +40 mV of varying durations, followed by a 100-ms prepulse to +40 mV to inactivate I_{to} and then a 100-ms test pulse to +40 mV. I_{Kur} displayed complete inactivation with conditioning pulses >20 s. In contrast, the original Courtemanche model-derived results showed little inactivation even with the longest conditioning-pulse duration (Fig. 1 *D*, *blue*). Conversely, the modified model closely replicated the experimental data (Fig. 1 *D*, *red*); the half-inactivation conditioning pulse duration ($CPD_{1/2}$) was 1100 ms at +40 mV. The voltage dependence of I_{Kur} inactivation was then assessed by applying a 50 s pretest pulse to various voltages followed by a 240-ms test pulse to +50 mV; the experimentally

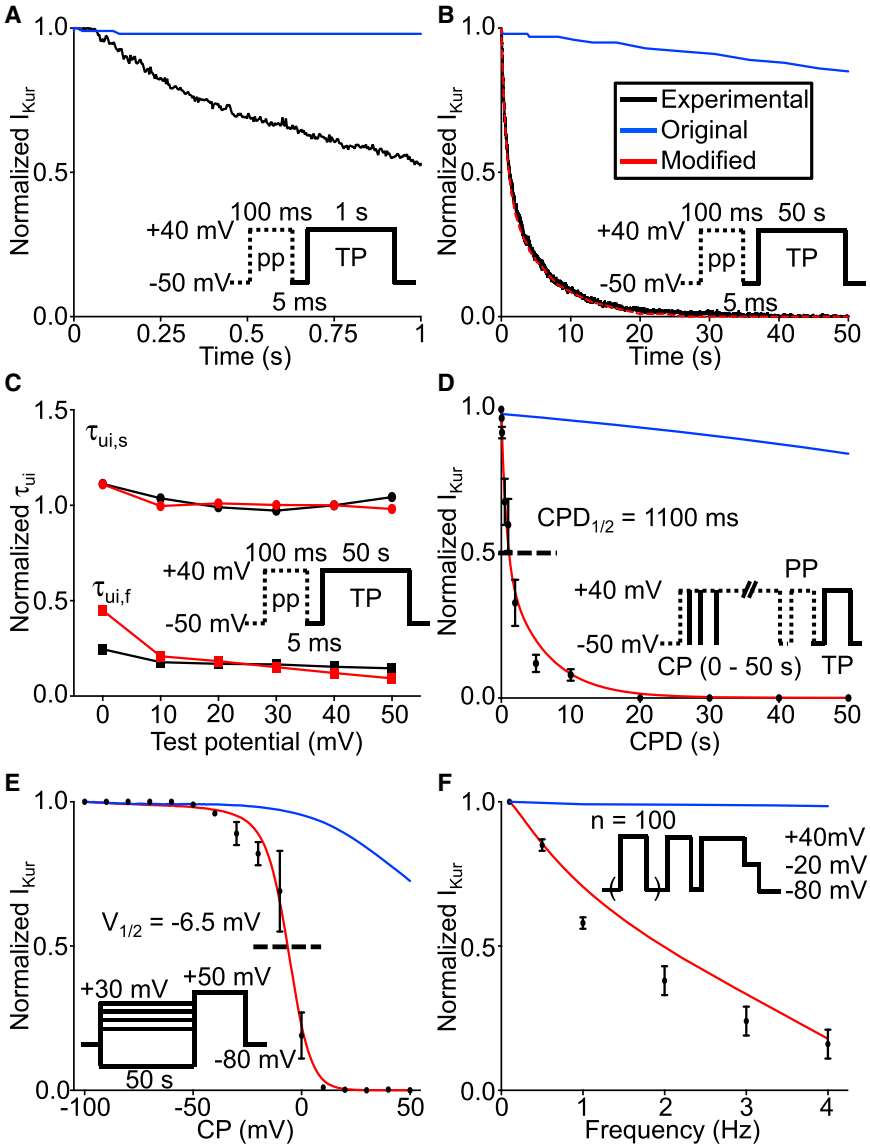

FIGURE 1 Time-, voltage-, and frequency dependence of I_{Kur} inactivation. (*A*) Shown here is the normalized I_{Kur} current during a 1000-ms test pulse (TP) at +40 mV, 5 ms after a 100-ms prepulse (PP), to inactivate I_{to} (*inset*) as recorded from the experimental preparation (*black*) and the original Courtemanche human atrial model (*blue*). (*B*) Normalized I_{Kur} current using a similar protocol, but with test pulse duration of 50 s as recorded from the experimental preparation (*black*) and the original and modified Courtemanche model (*blue* and *red*, respectively), is given. The experimental and modified model time constants are $\tau_{ui,f,exp}$ = 702 ± 7 ms, $\tau_{ui,s,exp}$ = 5688 ± 26 ms and $\tau_{ui,f,model}$ = 713 ± 18 ms, $\tau_{ui,s,model}$ = 5848 ± 188 ms, respectively. (*C*) Normalized fast ($\tau_{ui,f}$) and slow ($\tau_{ui,s}$) time constants as a function of test pulse potential for the experimental preparation and the modified Courtemanche model at 37°C are shown. (*D*) Shown here is the normalized I_{Kur} current using a CPD to +40 mV, followed by a 100-ms prepulse (PP) to +40 mV to inactivate I_{to} preceding a 100-ms test pulse (TP) to +40 mV (*inset*), as recorded from the experimental preparation and the original and modified models; the half-inactivation CPD ($CPD_{1/2}$) was 1100 ms. (*E*) Shown here is the normalized I_{Kur} current using a 50 s-conditioning pulse (CP) to various voltages followed by a 240-ms test pulse to +50 mV (*inset*); the half-inactivation voltage ($V_{1/2}$) was –6.5 mV in the model and –7.5 ± 0.6 mV experimentally. (*F*) Shown here is the normalized I_{Kur} current obtained by applying 100 pretest stimuli of 100 ms duration at +40 mV at various frequencies, followed by a 100-ms conditioning pulse to +40 mV to inactivate I_{to} and a 140-ms test pulse to +40 mV (*inset*); the normalized current at 4 Hz was 16% of its value at 0.1 Hz. For all panels, experimental data are in black; original and modified models are in blue and red, respectively.

recorded normalized I_{Kur} is shown in Fig. 1 *E* (*black*). I_{Kur} inactivation is highly dependent on the pretest pulse potential. The original Courtemanche model (*blue*) did not reproduce the experimentally observed voltage-dependent inactivation dependence (Fig. 1 *E*, *black*), whereas the modified model-generated results (*red*) closely matched experimental findings. The experimental and modified-model half-inactivation voltages ($V_{1/2}$s) were −7.5 ± 0.6 and −6.5 mV, respectively.

The frequency dependence of I_{Kur} inactivation was studied by applying 100 pulses of 100-ms duration to +40 mV at various frequencies, followed by a 100-ms conditioning pulse to +40 mV to inactivate I_{to} and a 140-ms test pulse to +40 mV. Experimentally, I_{Kur} displayed marked frequency dependence with 84% reduction at 4 vs. 0.1 Hz (Fig. 1 *F*, *black data*). In contrast, the original Courtemanche model showed virtually no frequency dependence (Fig. 1 *F*, *blue*). The modified model was much more consistent with the experimental findings (Fig. 1 *F*, *red*).

Incorporation of realistic I_{Kur} inactivation kinetics and AP dynamics

Fig. S2 shows the AP amplitude (Fig. S2 *A*), AP duration at 90% repolarization (APD_{90}, Fig. S2 *B*), transmembrane potential at the time of maximum phase 0 overshoot (overshoot potential, Fig. S2 *C*), and phase-0 peak Na^+ current (peak I_{Na}, Fig. S2 *D*) as a function of cycle length (CL) for the original (*black*) and modified (*red*) Courtemanche models. Despite markedly different I_{Kur} inactivation kinetics, there were no significant differences in AP or Na^+-current dynamics between the two models across a wide range of physiologically relevant cycle lengths. We then pursued the rate-dependent properties of I_{Kur} to understand why,

despite much greater inactivation for both experimental and model pulse protocols than in the original Courtemanche model, there was no apparent effect on rate-dependent AP properties.

I_{Kur} activation and inactivation dynamics and mechanisms of rate-dependence

Fig. 2 *A* shows model APs at progressively shorter stimulation cycle lengths (750, 500, 300, and 265 ms). The AP duration is shortened and plateau potential becomes less positive as the dome disappears when stimulation cycle length decreases. Fig. 2 *B* shows the corresponding I_{Kur} simulations. There is a rate-dependent decrease in I_{Kur} during phase 2 of the AP with little change in peak I_{Kur} (*inset*) except at the shortest cycle length (*inset*, *red*). Fig. 2, *C* and *D*, shows the corresponding activation and inactivation gate open probabilities (u_a^3; $u_{i,f} \times u_{i,s}$) as a function of time for the shortest (*red*) and longest (*blue*) cycle length. I_{Kur} activation decreases during phase 2 in a rate-dependent manner (Fig. 2 *C*), whereas inactivation is virtually rate independent (Fig. 2 *D*). Therefore, I_{Kur} rate dependence is driven by its activation gate kinetics, with little contribution from inactivation. This is further detailed in Fig. S3 where the rate dependence of the total I_{Kur} charge carried per cycle (Fig. S3 *B*) is shown to be due to changes in rate-dependent activation-gate open probability (Fig. S3 *F*), with no significant contribution from inactivation (Fig. S3 *D*).

Fig. 2 *E* shows the steady-state activation gating variable as a function of transmembrane potential with the voltage for 50% ($V_{0.5} = -30$ mV) activation marked with a purple dot; $V_{0.5}$ is shown in Fig. 2 *A* as a purple dashed line. For membrane potentials negative to $V_{0.5}$, the activation gate starts to close, whereas for potentials positive to $V_{0.5}$, the activation gate is mostly open. The activation-variable (u_a^3; Fig. 2 *C*) rate dependence can be understood based on the AP time course (Fig. 2 *A*) and u_a's voltage dependence (Fig. 2 *E*). At slower stimulation frequencies like a cycle length of 750 ms (*blue curve* in Fig. 2 *A*), the plateau potential is positive to $V_{0.5}$ (*dashed purple line* in Fig. 2 *A*) for the duration of phase 2 of the AP, keeping u_a largely open. It is only at the end of the AP plateau that the membrane potential falls below $V_{0.5}$, leading to appreciable decreases in u_a and return of the activation gate open probability toward 0 ($u_a^3 = 0$, *closed*, Fig. 2 *C*). In contrast, at faster stimulation frequencies such as at a cycle length of 265 ms (*red curve* in Fig. 2 *A*), the plateau potential is negative to $V_{0.5}$ starting at the end of phase 1 (Fig. 2 *A*), leading to earlier and more rapid closure of the activation gate (*red curve* in Fig. 2 *C*). The activation-gate time constant is in the range of 1–6 ms (Fig. S1 *D*), which allows the activation gate to closely track changes in membrane potential.

Fig. 2 *F* shows the fast ($u_{i,f}$, *solid black line*) and slow ($u_{i,s}$, *black dashed line*) inactivation gating variables as a function of test potential, with the slow inactivation-gating variable $V_{0.5}$ marked by a teal dot. For membrane potentials positive to $V_{0.5}$ (*teal dot*), the slow inactivation gate starts to close whereas for membrane potentials negative to $V_{0.5}$, the inactivation gates are mostly open. Fig. 2 *D* shows the inactivation gate open probability ($u_{i,f} \times u_{i,s}$) as a function of time at stimulation cycle lengths of 265 ms (*red*) and 750 ms (*blue*). The rate independence of $u_{i,f} \times u_{i,s}$ (Fig. 2 *D*,

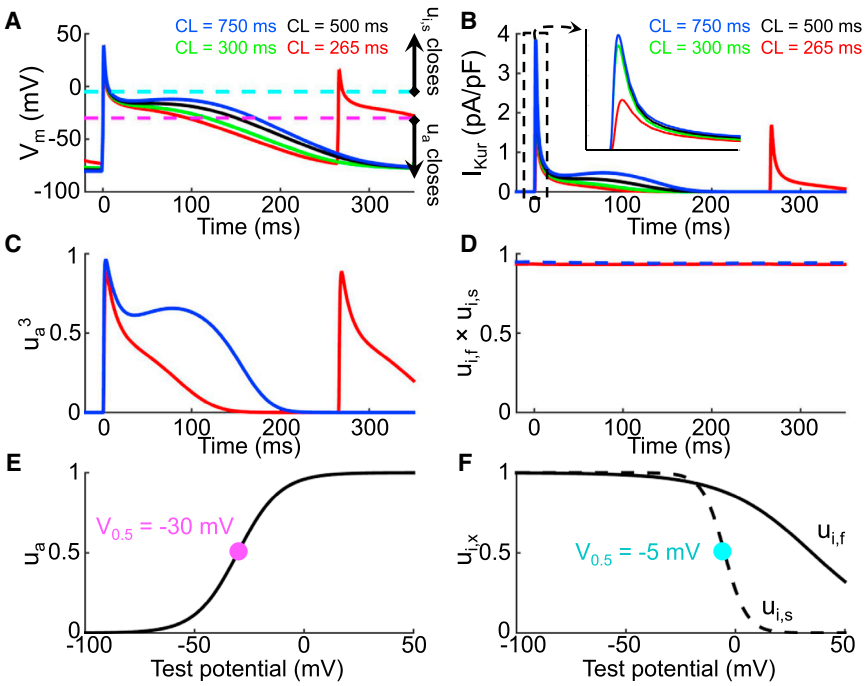

FIGURE 2 Mechanism of I_{Kur} rate dependence. (*A*) Action potentials at stimulation cycle lengths from 265 ms (*red*), 300 ms (*green*), 500 ms (*black*), and 750 ms (*blue*) are shown. The purple and teal dashed lines correspond to the activation and inactivation gating variable 50% ($V_{0.5,ua} = -30$ mV and $V_{0.5,uis} = -5$ mV) opening potentials, respectively. (*B*) Shown here are corresponding I_{Kur} tracings; there is a rate-dependent decrease in I_{Kur} during phase 2 of the AP. (*C*) Shown here is the activation gate open probability (u_a^3) and (*D*) inactivation gate open probability ($u_{i,f} \times u_{i,s}$) as a function of time for CLs of 265 ms (*red*) and 750 ms (*blue*). The activation open probability is rate dependent and the inactivation open probability is rate independent. (*E*) Shown here is the activation gating variable (u_a) as a function of transmembrane potential; the purple dot corresponds to activation gating variable $V_{0.5}$ as transposed on (*A*). (*F*) Fast ($u_{i,f}$; *black solid*) and slow ($u_{i,s}$; *black dashed*) inactivation gating variables as a function of transmembrane potential are given; the teal dot corresponds to the slow inactivation gating variable $V_{0.5}$ as transposed on (*A*). The inactivation open probability is rate independent because the action potential spends very little time positive to $V_{0.5,uis}$ (−5 mV; *teal*).

blue versus *red*) can be explained from the AP time course (Fig. 2 *A*) and u_i's voltage dependence (Fig. 2 *F*). For the slow inactivation gate to close, the membrane potential needs to be positive to $V_{0.5}$ (−5 mV). For the fast inactivation variable, the voltage dependence is even more positive. However, the AP, both at cycle lengths of 265 and 750 ms, spends negligible time at potentials positive to the $V_{0.5}$ of either fast or slow inactivation (positive to the *blue-dashed line* in Fig. 2 *E*). Moreover, the inactivation time constants are >1 s (Fig. S1 *B*), at least two orders-of-magnitude longer than the time the membrane spends above $V_{0.5}$. Hence, because the membrane spends very little time positive to $V_{0.5}$ and the inactivation gate time constants are slow to close, the inactivation gating variables remain mostly in their open state (>0.93 fractional availability, Fig. 2 *D*) irrespective of activation frequency.

Rate-dependent effects of I_{Kur} block on AP properties and underlying mechanism

When I_{Kur} is blocked, the plateau voltage is raised and I_{Kr} is enhanced, counteracting the repolarization delays caused by I_{Kur} block (8). Consequently, to understand the rate-dependent AP changes caused by I_{Kur} block, it is essential to analyze the associated changes in I_{Kr}. Fig. 3 *A* shows the steady-state I_{Kr} activation-gate variable in the Courtemanche model as a function of test potential, with $V_{0.1}$ (−28 mV), $V_{0.5}$ (−14 mV), $V_{0.75}$ (−7 mV), and $V_{0.9}$ (0 mV) marked and transposed as dashed lines onto Fig. 3 *B*. Fig. 3, *B–D*, shows the AP, I_{Kur}, and I_{Kr} simulations obtained at a cycle length of 1000 ms under control conditions (*blue*) and with 75% I_{Kur} block (*red*). I_{Kur} block elevates the plateau potential, bringing the membrane potential positive to I_{Kr}'s $V_{0.5}$ (−14 mV; *green dashed line* in Fig. 3 *B*) for the duration of phase 2 of the AP, leading to a 136% increase in I_{Kr}, an acceleration in phase-3 repolarization and no net change in overall APD (Fig. 3 *B*; APD_{-60} control versus I_{Kur} block = 255 vs. 256 ms, respectively). Fig. 3, *E–G*, shows the AP, I_{Kur}, and I_{Kr} simulations at a cycle length of 250 ms under control conditions (*blue*) and with 75% I_{Kur} block (*red*). Because of the change in AP morphology at the short cycle length, I_{Kur} block-induced elevation of the plateau fails to keep the plateau potential in the I_{Kr} activation range (e.g., $V_{0.5}$ of −14 mV; *green dashed line* in Fig. 3 *E*), hence, there is little I_{Kr} recruitment (ratio of total I_{Kr} with I_{Kur} block versus control = 1.40), leading to APD prolongation (APD_{-60} under control versus I_{Kur}-block conditions of 199 and 209 ms, respectively). Therefore, despite the fact that I_{Kur} is smaller at rapid frequencies, the ability of I_{Kur} block to prolong APD is enhanced.

I_{Kur} block and AF termination

The above analysis suggests that the APD-prolonging effect of I_{Kur} blockade is preserved at rapid rates and might result in an ability to suppress AF. We therefore studied the effect of I_{Kur} block on simulated two-dimensional cholinergic AF. We generated nine ACh conditions (Fig. S4); reentry was sustained for >5 s across conditions but displayed markedly different dynamics ranging from single spiral wave reentry (Fig. S5) to multiple, short-lived wavelets (Figs. 4, S5, and S6 for representative examples). In line with our single-cell results, there were no significant differences in reentry dynamics, APD_{-60} distribution, and depolarized

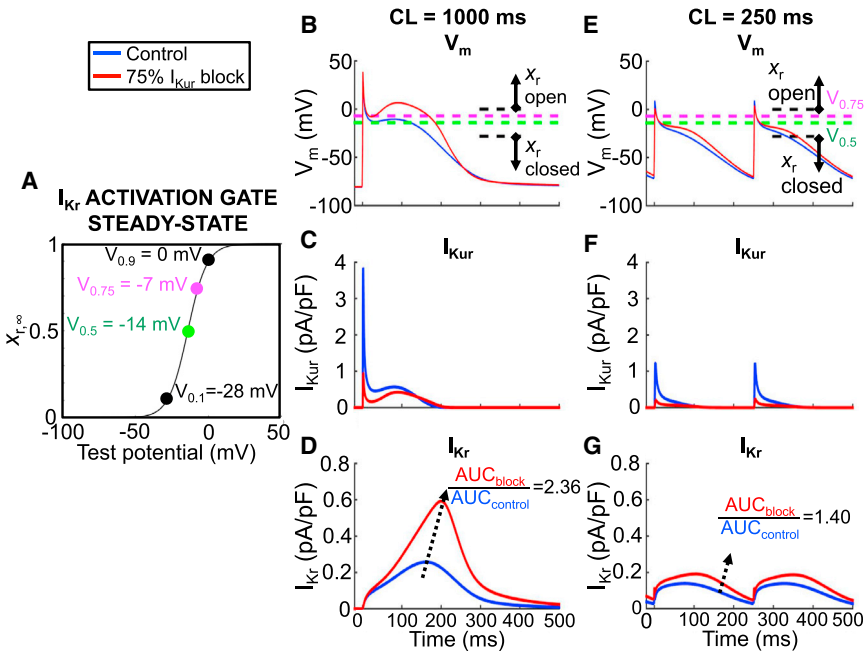

FIGURE 3 Rate-dependent effects of I_{Kur} block on the AP. (*A*) Shown here is the I_{Kr} activation gate steady state ($x_{r,\infty}$) as a function of test potential. $V_{0.1}$, $V_{0.5}$, $V_{0.75}$, and $V_{0.9}$ are marked and transposed onto (*B*) and (*E*) as dashed lines. (*B*) Shown here are APs obtained at a cycle length of 1000 ms under control (*blue*) and with 75% I_{Kur} blockade (*red*); the AP duration at −60 mV (APD_{-60}) was 255 ms for both. (*C* and *D*) Shown here are corresponding I_{Kur} and I_{Kr} tracings; the ratio of I_{Kr} with 75% I_{Kur} block to control was 2.36. (*E*) Shown here are APs obtained at a cycle length of 250 ms under control (*blue*) and with 75% I_{Kur} blockade (*red*); the APD_{-60} for control and 75% I_{Kur} block was 199 and 209 ms, respectively. (*F* and *G*) Shown here are corresponding I_{Kur} and I_{Kr} tracings; the ratio of I_{Kr} with 75% I_{Kur} block to control was 1.40.

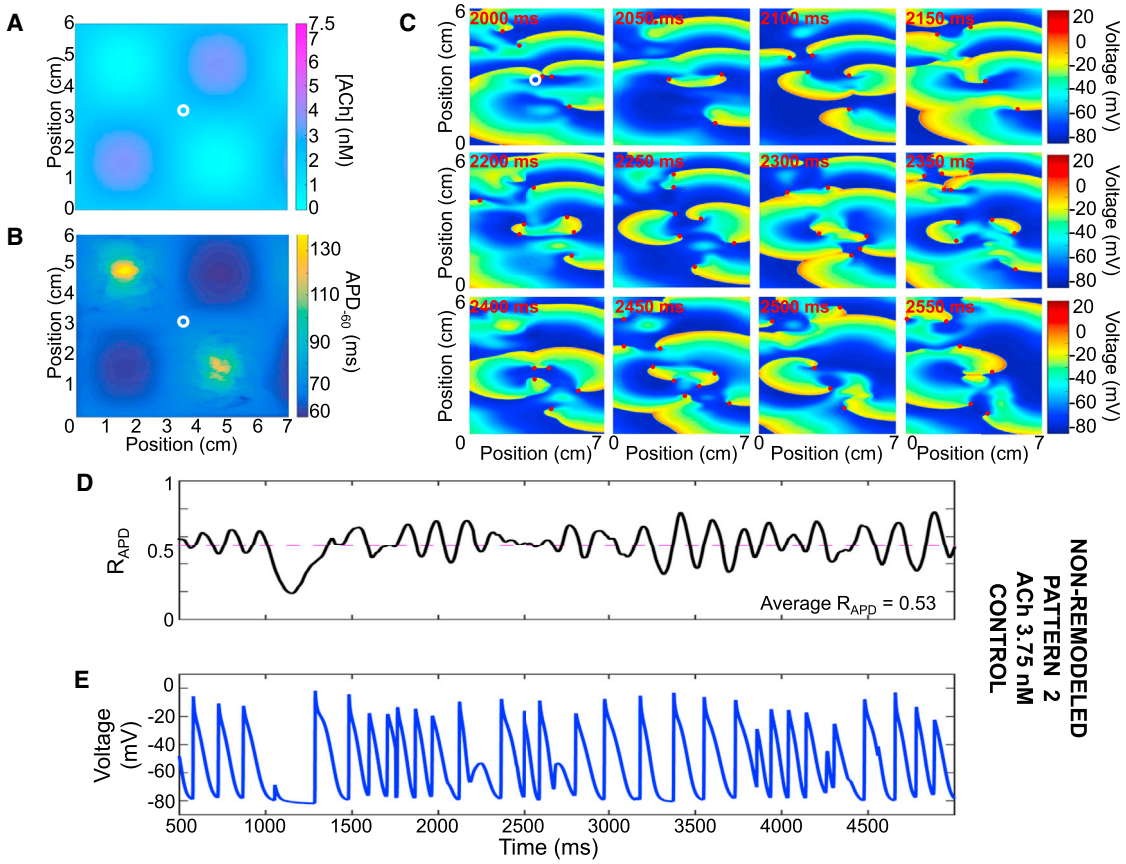

FIGURE 4 Representative example of simulated vagotonic AF using pattern #2 with a peak ACh concentration of 3.75 nM and the non-remodeled cardiomyocyte model. (*A*) Shown here is ACh distribution with peak concentration of 3.75 nM and (*B*) a corresponding APD_{-60} distribution. (*C*) Shown here is transmembrane potential over time at 50-ms intervals; reentry is maintained by multiple short-lived spiral waves. (*D*) Shown here is the ratio of depolarized cells (ratio of cells with a voltage positive to −60 mV to the total number of cells) and (*E*) transmembrane potential over time for the cardiomyocyte marked with a white circle in (*A*) and (*B*).

fraction between the original and modified I_{Kur} inactivation models (Figs. 5, S7, and S8 for representative examples). Using the non-remodeled Courtemanche human action potential model, we found a dose-dependent relationship between AF termination efficacy and percent I_{Kur} block (Fig. 6). Reentry termination was relatively infrequent with <50% I_{Kur} block, but increased to >90% of simulations at 100% I_{Kur} block for all conditions considered. We also found an inverse relationship between average time to termination and percent I_{Kur} block (Fig. 6).

Fig. 7 shows a representative example of successful AF termination by 50% I_{Kur} block with ACh pattern #2 and a peak concentration of 3.75 nM (Fig. 7 *A*). The areas of largest ACh concentration had the shortest APs (Fig. 7 *B*). I_{Kur} block prolonged refractoriness, increasing the excursion of the phase singularities, favoring wave-front collision, annihilation, and reentry termination (Fig. 7, *C–E*). Fig. S9 shows the dynamics with the same ACh pattern/concentration but with 100% I_{Kur} block; the increased refractoriness is even more pronounced and termination more rapid. Consistent with a significant role of I_{Kur} in AP repolarization, the mean APD_{-60} increased from 85 ms under control conditions to 97 and 126 ms at 50 and 100% I_{Kur} block, respectively.

We then sought to investigate whether I_{Kur} block could successfully terminate two-dimensional AF under ionically remodeled conditions, such as in chronic AF. As previously reported (7), AF-remodeling conditions stabilize reentry dynamics (Figs. S10–S12) and ACh is no longer needed to maintain AF. Overall, the efficacy of I_{Kur} block in terminating AF in remodeled atria was very low, with no termination observed below 80% block and 10% termination at 90 and 100% block in the absence of ACh and across the nine ACh conditions (see Fig. S13 for a representative example). At the cellular level, remodeling stabilized reentry 1) by significantly shortening the APD_{90} (APD_{90} for non-remodeled versus remodeled was 283 vs. 195 ms, respectively at CL 1000 ms and 204 vs. 140 ms, respectively at CL 250 ms) and 2) by hyperpolarizing the resting membrane potential (RMP) as compared to the non-remodeled cardiomyocyte (Fig. 8, *A* and *B*, *dashed* versus *solid*) across a wide range of diastolic intervals. The I_{Kur} block-induced APD_{90} prolongation was preserved under remodeled conditions (Fig. 8 *C* versus Fig. 8 *D*, *red* versus *blue*; ΔAPD_{90} at

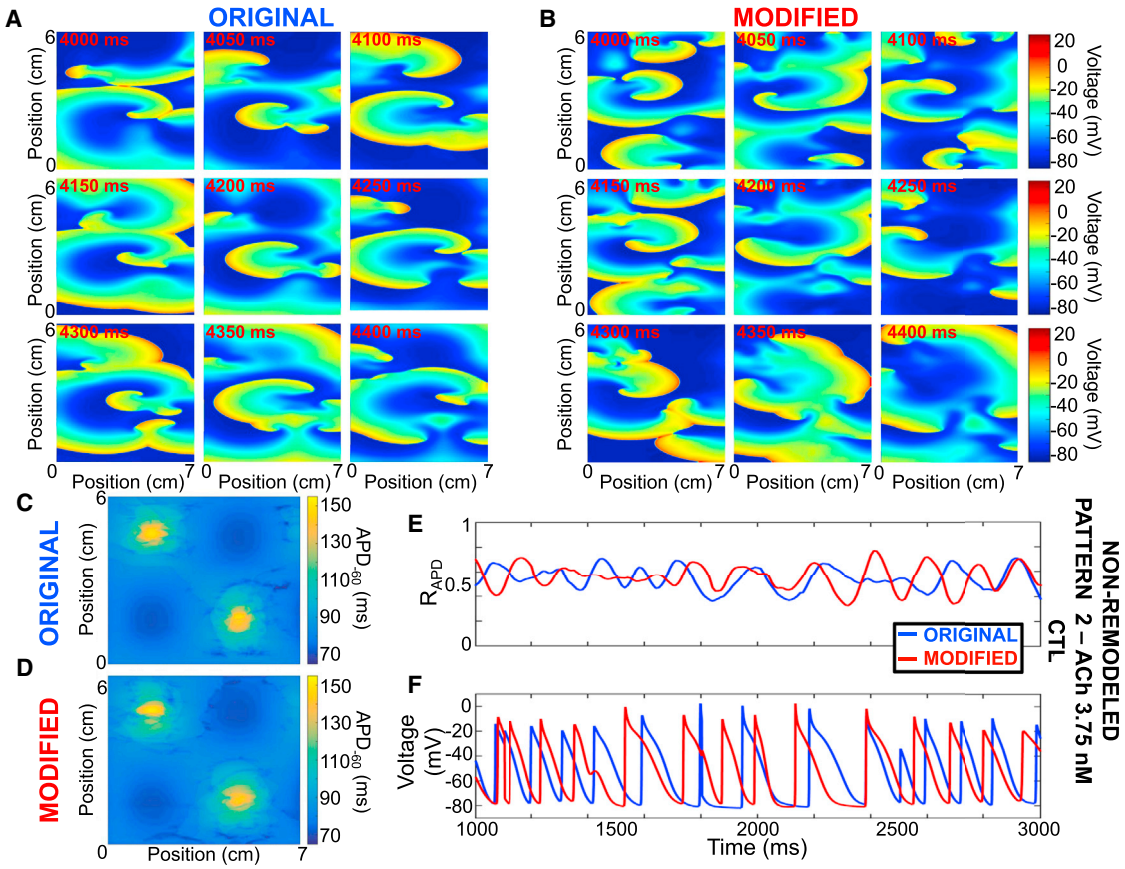

FIGURE 5 Representative example comparing reentry dynamics in the original and modified models. (*A* and *B*) Transmembrane potential snapshots over time at 50-ms intervals for the original and modified models are shown. (*C* and *D*) APD_{-60} values for the original and modified models are given. (*E* and *F*) Shown here is the ratio of depolarized cells (ratio of cells with a voltage positive to −60 mV to the total number of cells) and transmembrane potential for the original (*blue*) and modified (*red*) models. Non-remodeled cardiomyocyte model with ACh pattern #2 with peak concentration of 3.75 nM is given.

CL = 250 ms non-remodeled versus remodeled was 11 vs. 10 ms, respectively). However, because the remodeled AP is of much shorter duration and is hyperpolarized, the diastolic interval is long enough for the AP to return to the RMP before the next activation, even at rapid stimulation frequencies (Fig. 8 *A*, *blue* versus *red dashed*). Conversely, for the non-remodeled cardiomyocyte, even a small prolongation in APD encroaches on repolarization at short CLs (Fig. 8 *A*, *blue* versus *red solid*), and I_{Kur} block causes APD alternans behavior at short CLs (Fig. 8 *C*). Hence, the differential efficacy of I_{Kur} blockade for AF termination in remodeled versus non-remodeled atria appears to be related to the remodeling-induced APD-abbreviation and hyperpolarization more than from I_{Kur} downregulation, because the APD prolongation caused by I_{Kur} block is preserved in remodeled cardiomyocytes.

DISCUSSION

In this study, we have developed an updated formulation of I_{Kur} inactivation kinetics that reproduces experimentally observed I_{Kur} inactivation properties. Using the model, we have shown that, under physiological stimulation conditions, I_{Kur} dynamics are mainly determined by its activation kinetics with relatively minor contribution from channel inactivation. Hence, 1) contrary to intuition, I_{Kur} inactivation does not accumulate at rapid stimulation frequencies; and 2) despite a rate-dependent decrease in absolute I_{Kur} magnitude, the relative contribution of I_{Kur} to AP repolarization increases with increased activation frequency. We also found that I_{Kur} block terminates simulated cholinergic AF in a dose-dependent fashion in non-remodeled atrial tissue but is ineffective in the presence of simulated atrial remodeling. Because I_{Kur} is expressed in the human atrium but not ventricle (9), it is an interesting potential candidate for atrial-selective anti-AF therapy. Therefore, the demonstration that despite its potential for complete inactivation, I_{Kur} maintains a significant contribution to repolarization dynamics and arrhythmia maintenance during AF, is potentially important.

I_{Kur} inactivation

The initial reports characterizing I_{Kur} inactivation used relatively short test pulses, typically <5 s long, and therefore

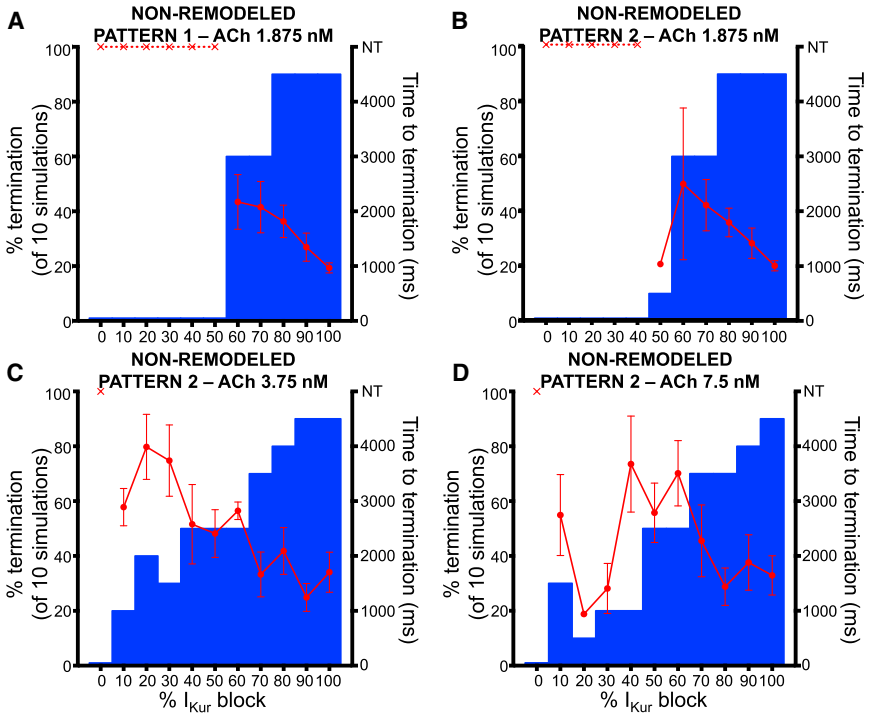

FIGURE 6 Dose-response (*bar-graphs*) and average time to termination (*red* data) by I_{Kur} block using the non-remodeled cardiomyocyte model for (*A*) ACh pattern #1 with peak ACh concentration of 1.875 nM. (*B–D*) Shown here are the ACh pattern #2 and peak ACh concentrations of 1.875, 3.75, and 7.5 nM, respectively.

failed to observe the full scale of I_{Kur} inactivation (1,10–14). Using 50-s test pulses, Feng et al. (2) demonstrated that human atrial I_{Kur} inactivates fully, with a biexponential time-course characterized by rapid and slow time constants of 1.0 and 6.8 s, respectively. Moreover, I_{Kur} inactivation was found to be highly time-, voltage-, and frequency-dependent. These observations raised the possibility that channel inactivation could accumulate at rapid activation frequencies, significantly decreasing I_{Kur}'s contribution to AP dynamics. If I_{Kur} inactivated completely at rapid activation frequencies, such as during AF, then I_{Kur} blockers would be predicted to have minimal antiarrhythmic effects. Paradoxically, and contrary to this intuitive expectation, recent work with the highly selective I_{Kur} blocker XEN-D0103 found that I_{Kur} block prolongs the atrial APD and effective refractory period preferentially at rapid activation frequencies (3).

Novel elements relative to prior in silico work

To our knowledge, none of the commonly used human atrial in silico models correctly reproduces the experimentally observed I_{Kur} inactivation kinetics. In this investigation, we first analyzed experimental recordings of I_{Kur} inactivation to produce an accurate in silico representation. We then studied I_{Kur} inactivation dynamics and rate-dependence with the updated model that accounted realistically for I_{Kur} inactivation (2) by introducing a set of fast and slow inactivation gating variables ($u_{i,f}$ and $u_{i,s}$) and corresponding time constants ($\tau_{ui,f}$ and $\tau_{ui,s}$). The modified model accurately reproduced I_{Kur} time-, voltage-, and frequency-dependent inactivation across a wide range of physiological test potentials. Of note, the inactivation-gate time constants are three orders-of-magnitude slower than the activation-gate time constant (second versus millisecond). After including the updated I_{Kur} representation in the Courtemanche AP-model, we compared AP parameters as a function of stimulation cycle length and found no significant difference between the original and modified model results despite markedly different inactivation kinetics. We then applied our model to gain insight into the role of I_{Kur} activation and inactivation on I_{Kur} and its rate-dependent role in repolarization and arrhythmia maintenance.

Mechanism of I_{Kur} rate dependence

Using the modified model, we showed that the activation gate open probability is highly rate-dependent (because of rate-induced AP morphology changes) and parallels I_{Kur} rate dependence, whereas the inactivation gate open probability is effectively rate independent because the cell spends little time at voltages associated with significant inactivation-gate closure. Hence, I_{Kur} rate-dependence is due to its activation gating-variable dynamics and rate-dependent changes in AP morphology, with no contribution from inactivation.

Rate-dependent effect of I_{Kur} block on AP repolarization

We next sought to understand the mechanism underlying the positive rate-dependent effect of I_{Kur} block on the APD, as

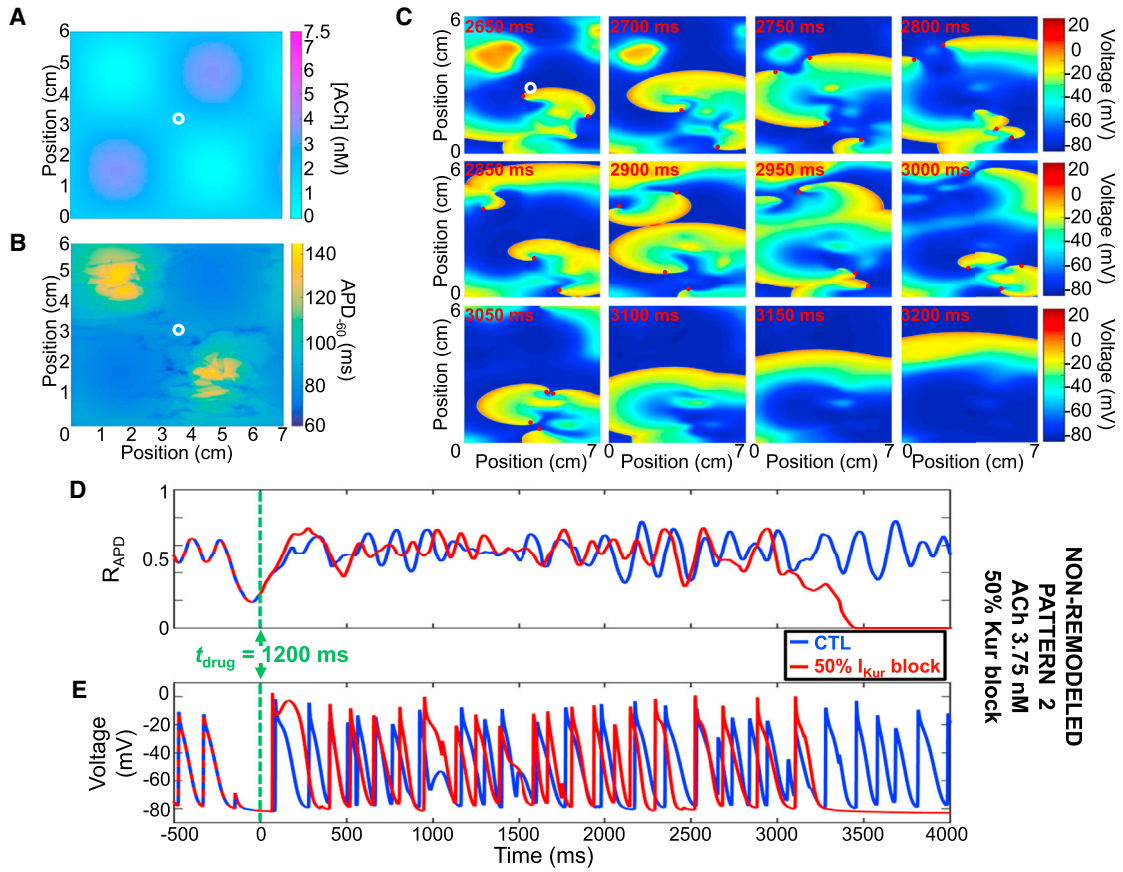

FIGURE 7 Representative example of reentry termination by 50% I_{Kur} block using ACh pattern #2 with peak ACh concentration of 3.75 nM and the non-remodeled cardiomyocyte model. (*A*)Shown here is the ACh distribution with peak concentration of 3.75 nM and (*B*) its corresponding APD_{-60} distribution. (*C*) Transmembrane potential snapshots over time at 50 ms intervals are given; 50% I_{Kur} block was introduced at $t_{drug} = 1200$ ms. (*D*) Shown here is the ratio of depolarized cells (ratio of cells with a voltage positive to −60 mV to the total number of cells) and (*E*) transmembrane potential over time for the cardiomyocyte marked with a white circle in (*A*) and (*B*) for control (*blue*) and 50% I_{Kur} block (*red*).

reported by Ford et al. (3). At slow stimulation frequencies, I_{Kur} block significantly elevated the AP plateau potential compared to control (no block), keeping the membrane at potentials for which I_{Kr}'s activation gate opens for the duration of phase 2 of the AP, leading to recruitment of I_{Kr} and compensating for I_{Kur} blockade with minimal effect on the APD. At rapid stimulation frequencies, the membrane potential is negative to I_{Kr}'s half-activation potential leading to little I_{Kr} recruitment, limited compensation by I_{Kr}, and I_{Kur} block-induced APD prolongation at rapid frequencies. Hence, although I_{Kur}'s absolute magnitude is less at rapid activation frequencies, the relative contribution of I_{Kur} to AP repolarization makes I_{Kur} block a potentially interesting atrial-selective anti-AF strategy.

The mechanisms of reverse rate-dependency (RRD) of drug-induced APD changes have been a matter of substantial debate. Arguing from first principles, Zaza (15) proposed that RRD is an intrinsic property of cardiac cells and that the same change in total transmembrane current will prolong long APs more than short ones. These predictions were supported by experimental work in which APD changes were shown to be proportional to the initial APD using clinically available drugs like the class-I agent lidocaine and class-III agent dofetilide, as well as by applying inward or outward current pulses (16). The same group suggested that channel blockers may, at best, attenuate this intrinsic RRD but that forward rate-dependency (FRD) would be "difficult to attain" (16). In an elegant study using a series of ventricular cardiomyocyte models, Cummins et al. (17) challenged this notion by suggesting that RRD can be overcome if rate-dependent AP morphological changes are large enough. In other words, the complex nonlinear rate-dependent changes in current dynamics may be such that RRD could be offset, making FRD possible. For example, they showed that increasing $I_{Ca,L}$ ($g_{Ca,L}$) leads to FRD changes by elevating the AP plateau potential, leading to differential I_{Ks} activation at slow activation frequencies (17). Because I_{Kur} is not expressed in ventricular cardiomyocytes, the possible FRD properties of I_{Kur} block could not be evaluated. Our findings in atrial cardiomyocytes are, however, qualitatively in line with these observations, because we found that I_{Kur} block moves the

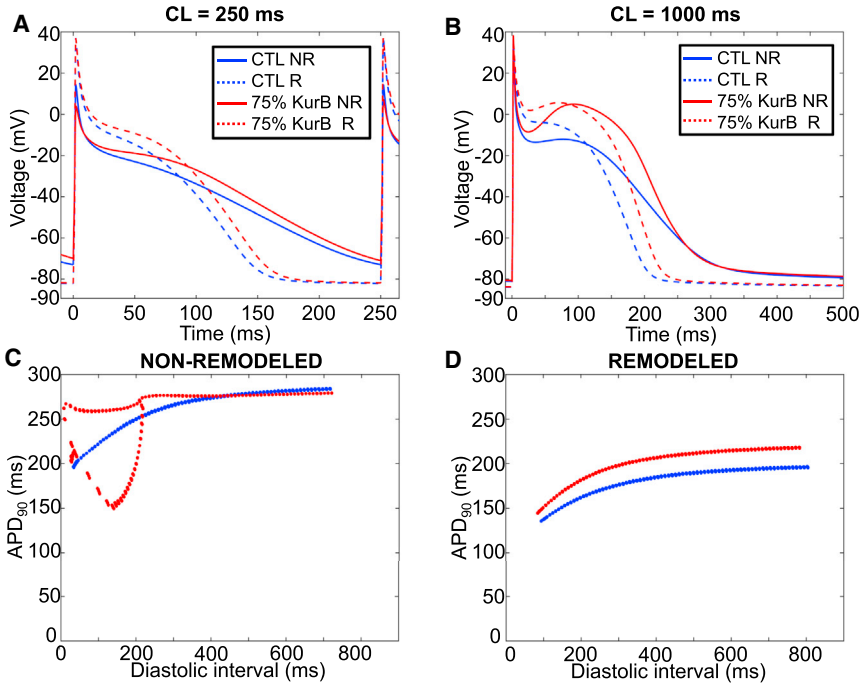

FIGURE 8 I_{Kur} blocking effects in remodeled cardiomyocytes. (*A*) Shown here is a single cell AP at a stimulation CL of 250 ms for a non-remodeled (NR; *solid*) and remodeled (R; *dashed*) cardiomyocyte without drug (*blue*) and with 75% I_{Kur} block (*red*); (*B*) same as in (*A*), but at CL of 1000 ms. (*C*) Shown here is an AP at 90% repolarization (APD_{90}) as a function of diastolic interval without drug (*blue*) and with 75% I_{Kur} block (*red*) for a non-remodeled cardiomyocyte; (*D*) same as in (*C*), but for a remodeled cardiomyocyte.

AP plateau potential to more positive voltages, leading to differential I_{Kr} activation at slow versus rapid pacing rates and FRD APD-prolongation. Hence, FRD APD-prolongation, a highly desirable antiarrhythmic property, may be an attainable goal.

Relevance for antiarrhythmic drug development

We also found that I_{Kur} block terminates simulated cholinergic AF in a dose-dependent manner in nonionically remodeled atrial tissue by prolonging refractoriness, increasing the reentry wavelength, favoring rotor collision and annihilation. These findings are consistent with prior experimental work using relatively I_{Kur}-specific blockers in goats, rats, pigs, humans, and in silico systems (18–22). Electrical remodeling shortened the APD and hyperpolarized the RMP, leading to very stable reentry as described in Pandit et al. (7). The ability of I_{Kur} block to terminate simulated AF was greatly attenuated by remodeling, because the block-induced APD-prolongation was insufficient to counteract the strong effects of remodeling. The APD-prolonging effect of I_{Kur} block was not per se affected by channel downregulation. These observations are consistent with the report by Ford et al. (3), in which APD_{90} prolongation induced by the I_{Kur}-selective blocker XEN-D0103 was maintained in chronic-AF human atrial cardiomyocytes. Scholz et al. (22) found that I_{Kur} block was effective at terminating simulated AF, even in remodeled atria. However, they used slightly different remodeling parameters, included gap junction remodeling, and did not incorporate I_{Kur} downregulation. The differential effectiveness of I_{Kur} block in non-remodeled versus remodeled atria is consistent with a prior randomized phase-3 clinical trial in which vernakalant, a mixed I_{Na}/I_{Kur} blocker, was much less effective at restoring sinus rhythm in patients with long-lasting AF (4.0%) compared to recent-onset AF (51.7%) (23). Of note, recent experimental work demonstrated persistent antiarrhythmic efficacy of vernakalant in goats with remodeled atria owing to unaltered effects on Na^+-dependent parameters (conduction velocity and postrepolarization refractoriness) (24). Our findings suggest that the clinical efficacy of pure I_{Kur} block may be limited to recent-onset AF, in which remodeling has not taken place.

For the purposes of this study, I_{Kur} block was simulated as a fixed reduction in maximal conductance (g_{Kur}). However, there is in silico and experimental evidence that the electrophysiological and antiarrhythmic effects of I_{Kur} blockade are modulated by the time- and voltage-dependent kinetics of block. Using a family of I_{Kur}-selective diphenyl phosphine oxide compounds, Lagrutta et al. (25) were able to show that I_{Kur} blocking potency and frequency dependence were functions of blocking kinetics, with open state blockers being the most effective I_{Kur} antagonists. Several other molecules, including vernakalant and experimental compounds like zatebradine, loratadine, and bisindolylmaleimide, have also been shown to block I_{Kur} preferentially in the open state (19,26–28). Mathematical simulations support these findings and suggest that I_{Kur} blockers with rapid binding or slow unbinding kinetics have the strongest antiarrhythmic effects (22,29). Further work is needed to analyze the effects (if any) on state-dependent drug block, of adding realistic I_{Kur} inactivation kinetics.

Consistent with this study, XEN-D0101, a selective I_{Kur} blocker, prolonged the atrial effective refractory period (AERP) and decreased AF vulnerability in a dose- and rate-dependent manner in atrial tachycardia-induced remodeled canine atria (30,31). In human cardiomyocytes, XEN-D0101 prolonged AERP in AF-remodeled but not in non-remodeled tissue (32). However, experiments were conducted using a stimulation frequency of 1 Hz at which we predict no effect on APD and AERP based on this study; rapid stimulation rates at which I_{Kur}-block induced prolongation of APD/atrial refractoriness would be expected were not reported. In coronary-perfused canine atria, 4-aminopyridine (a moderately selective I_{Kur} blocker) was found to shorten APD and to increase the propensity for AF, displaying only mildly antiarrhythmic effects in remodeled atrial tissue (33). Again, the protocol employed a stimulation cycle length of 500 ms at which I_{Kur} block would not be expected to increase the APD or AERP. Furthermore, the mechanism of I_{Kur} in dog atrium is different from that in humans, and the magnitude is often very small (34). MK-0448 failed to prolong AERP in healthy human subjects using relatively slow stimulation cycle lengths of 400 and 600 ms at which I_{Kr} recruitment balances I_{Kur} block (35). I_{Kur} block rate-dependence, as described in this study, along with species- and remodeling-related differences, likely account for these conflicting results. Finally, genetic studies reported both loss- and gain-of-function variants associated with the development of lone AF (36–39). Whether and how these observations in rare genetically based forms of AF are applicable, remains to be seen more broadly.

Na^+ channel blockers (NCBs) are moderately effective antiarrhythmic drugs commonly used to control AF (40). In 2015, it was reported that I_{Kr} block increases the anti-AF effects of an optimized NCB by delaying repolarization at rapid rates (41). However, I_{Kr} blockers have reverse-use-dependent effects on APD, such that the APD-prolonging effect of I_{Kr} block is maximal at the slow rates of normal sinus rhythm (producing a serious risk of excess repolarization delay and ventricular proarrhythmia) and decreases markedly at rapid rates like those of AF. Given the positive rate-dependence of the APD-prolonging effect of I_{Kur} block, the addition of an I_{Kur} blocker to an optimized NCB would be expected to potentiate the NCB's anti-AF efficacy preferentially at rapid rates such as during AF. We have already shown evidence for this principle in a canine computational model (41). The work presented here provides tools and further rationale for testing this concept in human models.

Study limitations

First, this study was performed in silico with extensive use of prior primary experimental patch-clamp data (2). The model predictions regarding the rate-dependent effects of I_{Kur} block on AP properties need to be tested prospectively in human tissue. Second, the model does not consider I_{Kur} modulation by adrenergic (42) or by vagal (30) tone, nor by temperature dependence (2). However, the model was based on data obtained at normal body temperature and should therefore be relevant to normal clinical conditions. Finally, as discussed above, we simulated I_{Kur} block with a fixed reduction in maximal conductance, whereas I_{Kur} block by antiarrhythmic drugs have been shown to depend on blocking kinetics and show state-dependent properties (22,29,43). Further computational analyses considering the state-dependent actions of specific I_{Kur} blockers might therefore be of interest.

Our simulations in remodeled atria have one major limitation. To compare remodeled results with those in non-remodeled conditions, we used the same I_{KACh} model and distributions. However, I_{KACh} is greatly reduced in remodeled atria (44). There are no realistic I_{KACh} models for remodeled atria. Future work is needed to create such models and use them to obtain a more accurate picture of I_{Kur}-blocking effects under these conditions.

CONCLUSIONS

An updated in silico model that accounts for experimentally observed I_{Kur} inactivation kinetics shows that, contrary to possible intuitive inferences based on the potentially complete inactivation shown by I_{Kur}, I_{Kur} inactivation is in fact negligible under physiologically relevant conditions. On the contrary, the main determinant of I_{Kur} rate dependence is the response of its activation dynamics to frequency-dependent changes in AP-morphology. However, despite a smaller absolute I_{Kur} magnitude at rapid rates, the relative contribution of I_{Kur} to AP repolarization increases because of decreases in offsetting currents, particularly I_{Kr}. These positive rate-dependent effects allow I_{Kur} block to terminate AF and position it to have potentially valuable antiarrhythmic properties. At the same time, our results also suggest that the efficacy of I_{Kur} block for AF termination might be greatly attenuated in the ionically remodeled atrium that develops after several days or more of sustained AF (8).

SUPPORTING MATERIAL

Thirteen figures are available at http://www.biophysj.org/biophysj/supplemental/S0006-3495(17)30341-7.

AUTHOR CONTRIBUTIONS

M.A. designed the study with the assistance of P.C. and S.N., performed all the simulations, analyzed the data and composed the manuscript. J.F. performed the original experimental work, provided all the original experimental data for analysis, and helped with the interpretation of the experimental results. E.V. provided the code for the AF simulation and assisted in its execution/analysis. P.C. supervised the modeling work and provided comments to improve the manuscript. S.N. supervised all aspects of the work, contributed to the original study concept and design, and helped with planning and completion of the manuscript.

ACKNOWLEDGMENTS

We thank Jennifer Bacchi for expert secretarial assistance with the manuscript.

We acknowledge support through the Canadian Institutes of Health Research and Quebec Heart Foundation (S.N.), the Natural Sciences and Engineering Research Council (P.C.), and the Agence National de Recherche de France through the Investissements d'Avenir Program No. ANR-10-IAHU-04 (E.V.). Computations were made on the supercomputer Briare from Université de Montréal, managed by Calcul Québec and Compute Canada. The operation of this supercomputer is funded by the Canada Foundation for Innovation (CFI), the ministère de l'Économie, de la science et de l'innovation du Québec (MESI), and the Fonds de recherche du Québec - Nature et technologies (FRQ-NT).

REFERENCES

1. Wang, Z., B. Fermini, and S. Nattel. 1993. Sustained depolarization-induced outward current in human atrial myocytes. Evidence for a novel delayed rectifier K^+ current similar to Kv1.5 cloned channel currents. *Circ. Res.* 73:1061–1076.
2. Feng, J., D. Xu, …, S. Nattel. 1998. Ultrarapid delayed rectifier current inactivation in human atrial myocytes: properties and consequences. *Am. J. Physiol.* 275:H1717–H1725.
3. Ford, J., J. Milnes, …, U. Ravens. 2016. The positive frequency-dependent electrophysiological effects of the I_{Kur} inhibitor XEN-D0103 are desirable for the treatment of atrial fibrillation. *Heart Rhythm.* 13: 555–564.
4. Courtemanche, M., R. J. Ramirez, and S. Nattel. 1998. Ionic mechanisms underlying human atrial action potential properties: insights from a mathematical model. *Am. J. Physiol.* 275:H301–H321.
5. Kneller, J., R. Zou, …, S. Nattel. 2002. Cholinergic atrial fibrillation in a computer model of a two-dimensional sheet of canine atrial cells with realistic ionic properties. *Circ. Res.* 90:E73–E87.
6. Vigmond, E. J., M. Hughes, …, L. J. Leon. 2003. Computational tools for modeling electrical activity in cardiac tissue. *J. Electrocardiol.* 36:69–74.
7. Pandit, S. V., O. Berenfeld, …, J. Jalife. 2005. Ionic determinants of functional reentry in a 2-D model of human atrial cells during simulated chronic atrial fibrillation. *Biophys. J.* 88:3806–3821.
8. Courtemanche, M., R. J. Ramirez, and S. Nattel. 1999. Ionic targets for drug therapy and atrial fibrillation-induced electrical remodeling: insights from a mathematical model. *Cardiovasc. Res.* 42:477–489.
9. Feng, J., B. Wible, …, S. Nattel. 1997. Antisense oligodeoxynucleotides directed against Kv1.5 mRNA specifically inhibit ultrarapid delayed rectifier K^+ current in cultured adult human atrial myocytes. *Circ. Res.* 80:572–579.
10. Philipson, L. H., R. E. Hice, …, D. F. Steiner. 1991. Sequence and functional expression in *Xenopus* oocytes of a human insulinoma and islet potassium channel. *Proc. Natl. Acad. Sci. USA.* 88:53–57.
11. Snyders, D. J., M. M. Tamkun, and P. B. Bennett. 1993. A rapidly activating and slowly inactivating potassium channel cloned from human heart. Functional analysis after stable mammalian cell culture expression. *J. Gen. Physiol.* 101:513–543.
12. Firek, L., and W. R. Giles. 1995. Outward currents underlying repolarization in human atrial myocytes. *Cardiovasc. Res.* 30:31–38.
13. Amos, G. J., E. Wettwer, …, U. Ravens. 1996. Differences between outward currents of human atrial and subepicardial ventricular myocytes. *J. Physiol.* 491:31–50.
14. Koidl, B., P. Flaschberger, …, B. Rigler. 1996. Effects of the class III antiarrhythmic drug ambasilide on outward currents in human atrial myocytes. *Naunyn Schmiedebergs Arch. Pharmacol.* 353:226–232.
15. Zaza, A. 2010. Control of the cardiac action potential: the role of repolarization dynamics. *J. Mol. Cell. Cardiol.* 48:106–111.
16. Bányász, T., B. Horváth, …, P. P. Nánási. 2009. Reverse rate dependency is an intrinsic property of canine cardiac preparations. *Cardiovasc. Res.* 84:237–244.
17. Cummins, M. A., P. J. Dalal, …, E. A. Sobie. 2014. Comprehensive analyses of ventricular myocyte models identify targets exhibiting favorable rate dependence. *PLoS Comput. Biol.* 10:e1003543.
18. Knobloch, K., J. Brendel, …, K. J. Wirth. 2002. Electrophysiological and antiarrhythmic effects of the novel I_{Kur} channel blockers, S9947 and S20951, on left vs. right pig atrium in vivo in comparison with the I_{Kr} blockers dofetilide, azimilide, d,l-sotalol and ibutilide. *Naunyn-Schiedeberg's Arch. Pharmacol.* 366:482–487.
19. Blaauw, Y., H. Gögelein, …, M. A. Allessie. 2004. "Early" class III drugs for the treatment of atrial fibrillation: efficacy and atrial selectivity of AVE0118 in remodeled atria of the goat. *Circulation.* 110: 1717–1724.
20. Fedida, D., P. M. R. Orth, …, G. N. Beatch. 2005. The mechanism of atrial antiarrhythmic action of RSD1235. *J. Cardiovasc. Electrophysiol.* 16:1227–1238.
21. Dorian, P., A. Pinter, …, G. N. Beatch. 2007. The effect of vernakalant (RSD1235), an investigational antiarrhythmic agent, on atrial electrophysiology in humans. *J. Cardiovasc. Pharmacol.* 50:35–40.
22. Scholz, E. P., P. Carrillo-Bustamante, …, G. Seemann. 2013. Rotor termination is critically dependent on kinetic properties of I_{Kur} inhibitors in an in silico model of chronic atrial fibrillation. *PLoS One.* 8:e83179.
23. Roy, D., C. M. Pratt, …, A. J. Camm; Atrial Arrhythmia Conversion Trial Investigators. 2008. Vernakalant hydrochloride for rapid conversion of atrial fibrillation: a phase 3, randomized, placebo-controlled trial. *Circulation.* 117:1518–1525.
24. van Hunnik, A., D. H. Lau, …, U. Schotten. 2016. Antiarrhythmic effect of vernakalant in electrically remodeled goat atria is caused by slowing of conduction and prolongation of postrepolarization refractoriness. *Heart Rhythm.* 13:964–972.
25. Lagrutta, A., J. Wang, …, J. J. Salata. 2006. Novel, potent inhibitors of human Kv1.5 K^+ channels and ultrarapidly activating delayed rectifier potassium current. *J. Pharmacol. Exp. Ther.* 317:1054–1063.
26. Valenzuela, C., E. Delpón, …, D. J. Snyders. 1996. Class III antiarrhythmic effects of zatebradine. Time-, state-, use-, and voltage-dependent block of hKv1.5 channels. *Circulation.* 94:562–570.
27. Delpón, E., C. Valenzuela, …, J. Tamargo. 1997. Block of human cardiac Kv1.5 channels by loratadine: voltage-, time- and use-dependent block at concentrations above therapeutic levels. *Cardiovasc. Res.* 35:341–350.
28. Choi, B. H., J.-S. Choi, …, M.-S. Kim. 2000. Direct block by bisindolylmaleimide of rat Kv1.5 expressed in Chinese hamster ovary cells. *J. Pharmacol. Exp. Ther.* 293:634–640.
29. Tsujimae, K., S. Suzuki, …, Y. Kurachi. 2007. Frequency-dependent effects of various I_{Kr} blockers on cardiac action potential duration in a human atrial model. *Am. J. Physiol. Heart Circ. Physiol.* 293: H660–H669.
30. Rivard, L., A. Shiroshita-Takeshita, …, S. Nattel. 2005. Electrophysiological and atrial antiarrhythmic effects of a novel I_{Kur}/Kv1.5 blocker in dogs. *Heart Rhythm.* 2:S180.
31. Shiroshita-Takeshita, A., C. Maltais, …, S. Nattel. 2006. Electrophysiological and atrial antiarrhythmic effects of a novel I_{Kur}/Kv1.5 blocker in dogs with atrial tachycardia remodeling. *Heart Rhythm.* 3:S183.
32. Ford, J., J. Milnes, …, U. Ravens. 2013. Human electrophysiological and pharmacological properties of XEN-D0101: a novel atrial-selective Kv1.5/I_{Kur} inhibitor. *J. Cardiovasc. Pharmacol.* 61:408–415.
33. Burashnikov, A., and C. Antzelevitch. 2008. Can inhibition of I_{Kur} promote atrial fibrillation? *Heart Rhythm.* 5:1304–1309.
34. Yue, L., Z. Wang, …, S. Nattel. 2000. Molecular evidence for a role of *Shaw* (Kv3) potassium channel subunits in potassium currents of dog atrium. *J. Physiol.* 527:467–478.

35. Pavri, B. B., H. E. Greenberg, …, D. Bloomfield. 2012. MK-0448, a specific Kv1.5 inhibitor: safety, pharmacokinetics, and pharmacodynamic electrophysiology in experimental animal models and humans. *Circ. Arrhythm. Electrophysiol.* 5:1193–1201.

36. Olson, T. M., A. E. Alekseev, …, A. Terzic. 2006. Kv1.5 channelopathy due to KCNA5 loss-of-function mutation causes human atrial fibrillation. *Hum. Mol. Genet.* 15:2185–2191.

37. Yang, T., P. Yang, …, D. Darbar. 2010. Novel KCNA5 mutation implicates tyrosine kinase signaling in human atrial fibrillation. *Heart Rhythm.* 7:1246–1252.

38. Christophersen, I. E., M. S. Olesen, …, N. Schmitt. 2013. Genetic variation in KCNA5: impact on the atrial-specific potassium current I_{Kur} in patients with lone atrial fibrillation. *Eur. Heart J.* 34:1517–1525.

39. Hayashi, K., T. Konno, …, M. Yamagishi. 2015. Functional characterization of rare variants implicated in susceptibility to lone atrial fibrillation. *Circ. Arrhythm. Electrophysiol.* 8:1095–1104.

40. Aguilar, M., and S. Nattel. 2015. The past, present, and potential future of sodium channel block as an atrial fibrillation suppressing strategy. *J. Cardiovasc. Pharmacol.* 66:432–440.

41. Aguilar, M., F. Xiong, …, S. Nattel. 2015. Potassium channel blockade enhances atrial fibrillation-selective antiarrhythmic effects of optimized state-dependent sodium channel blockade. *Circulation.* 132:2203–2211.

42. Li, G. R., J. Feng, …, S. Nattel. 1996. Adrenergic modulation of ultrarapid delayed rectifier K^+ current in human atrial myocytes. *Circ. Res.* 78:903–915.

43. Almquist, J., M. Wallman, …, M. Jirstrand. 2010. Modeling the effect of Kv1.5 block on the canine action potential. *Biophys. J.* 99:2726–2736.

44. Dobrev, D., E. Graf, …, U. Ravens. 2001. Molecular basis of downregulation of G-protein-coupled inward rectifying K^+ current ($I_{K,Ach}$) in chronic human atrial fibrillation: decrease in GIRK4 mRNA correlates with reduced ($I_{K,Ach}$) and muscarinic receptor-mediated shortening of action potentials. *Circulation.* 104:2551–2557.

Biophysical Journal, Volume *112*

Supplemental Information

Rate-Dependent Role of I_{Kur} in Human Atrial Repolarization and Atrial Fibrillation Maintenance

Martin Aguilar, Jianlin Feng, Edward Vigmond, Philippe Comtois, and Stanley Nattel

SUPPORTING MATERIAL: FIGURE LEGENDS

Figure S1. Model inactivation and activation gating variables and time constants. (A) Inactivation gating variable as a function of transmembrane potential (V_m) for the original model ($u_{i,original}$; blue) and fast ($u_{i,f}$, red solid) and slow ($u_{i,s}$, red dashed) inactivation gating variables for the modified model. (B) Inactivation time constants as a function of transmembrane potential for the original ($\tau_{ui,original}$, blue) and modified ($\tau_{ui,f}$, red sold; $\tau_{ui,s}$, red dashed) model. (C) Activation gating variable as a function of transmembrane potential for the original ($u_{a,original}$, blue) and modified ($u_{a,modified}$, red) model. (D) Activation time constant as a function of transmembrane potential for the original ($\tau_{ua,original}$, blue) and modified ($\tau_{ua,modified}$, red) model.

Figure S2. I_{Kur} inactivation and action potential dynamics. (A) Action potential amplitude (APA), (B) action potential duration at 90% repolarizaton (APD_{90}), (C) maximal phase-0 overshoot potential (OS) and (D) peak Na^+ current (peak I_{Na}) as a function of stimulation cycle length (CL) for the original (black) and modified (red) Courtemanche models.

Figure S3. Left panels: Kinetic determinants of I_{Kur} at a cycle length of 750 ms. Right panels: Cycle-length dependence of the same kinetic determinants (points corresponding to a cycle length of 750 ms indicated by an X). (A) Determinants of I_{Kur} rate dependence as a function of time for a stimulation cycle length (CL) of 750 ms. The area under the I_{Kur} curve (I_{Kur} AUC; shaded red) is calculated to determine charge carried per cycle. (B) I_{Kur} AUC as a function of stimulation cycle length. (C) Inactivation gate open probability ($u_{i,f} \times u_{i,s}$) as a function of time at CL = 750 ms. The open-probability minimum is marked by a red dot. (D) Inactivation gate open probability minima as a function of cycle length. (E) Activation gate open probability (u_a^3) as a function of time at CL = 750 ms. The area under the u_a^3 curve (u_a^3 AUC) is shaded in red). (F) Activation gate open probability AUC (u_a^3 AUC) as a function of stimulation cycle length.

Figure S4. ACh distributions used for the 2-dimensional AF simulations. Pattern #1 is a flat ACh distribution. Pattern #2 and #3 are sinusoidal ACh distributions. Three peak ACh concentrations (1.875 nM, 3.75 nM and 7.5 nM) for each pattern generated 9 different substrate conditions.

Figure S5. Representative example of simulated cholinergic AF using pattern #1 with peak ACh concentration of 7.5 nM and the non-remodeled cardiomyocyte model. (A) ACh distribution with peak concentration of 7.5 nM and (B) corresponding APD_{-60} distribution. (C) Transmembrane potential over time at 50 ms intervals; re-entry is very stable and maintained by a single rotor. (D) Ratio of depolarized cells and (E) transmembrane potential over time for the cardiomyocyte marked with a white circle in panels A and B.

Figure S6. Representative example of simulated cholinergic AF using pattern #3 with peak ACh concentration of 7.5 nM and the non-remodeled cardiomyocyte model. (A) ACh distribution with peak concentration of 7.5 nM and (B) corresponding APD_{-60} distribution. (C) Transmembrane potential over time at 50 ms intervals; re-entry is maintained by multiple short-live spiral waves. (D) Ratio of depolarized cells and (E) transmembrane potential over time for the cardiomyocyte marked with a white circle in panels A and B.

Figure S7. Representative example comparing re-entry dynamics in the original and modified models. (A-B) Transmembrane potential over time at 50 ms intervals for the original and modified models. (C-D) APD-60 for the original and modified models. (E-F) Ratio of depolarized cells and transmembrane potential for the original (blue) and modified (red) models. Non-remodeled cardiomyocyte model with ACh pattern #1 with peak concentration of 1.875 nM.

Figure S8. Representative example comparing re-entry dynamics in the original and modified models. (A-B) Transmembrane potential over time at 50 ms intervals for the original and modified models. (C-D) APD-60 for the original and modified models. (E-F) Ratio of depolarized cells and transmembrane potential for the original (blue) and modified (red) models. Non-remodeled cardiomyocyte model with ACh pattern #3 with peak concentration of 3.75 nM.

Figure S9. Representative example of re-entry termination by 100% I_{Kur} block using ACh pattern #2 with peak ACh concentration of 3.75 nM and the non-remodeled cardiomyocyte model. (A) ACh distribution with peak concentration of 3.75 nM and (B) corresponding APD_{-60} distribution. (C) Transmembrane potential over time at 50 ms intervals; 50% I_{Kur} block was introduced at t_{drug} = 1600 ms. (D) Ratio of depolarized cells and (E) transmembrane potential over time for the cardiomyocyte marked with a white circle in panels A and B for control (blue) and 50% I_{Kur} block (red).

Figure S10. Representative example of simulated cholinergic AF using pattern #1 with peak ACh concentration of 3.75 nM and the remodeled cardiomyocyte model. (A) ACh distribution with peak concentration of 3.75 nM and (B) corresponding APD_{-60} distribution. (C) Transmembrane potential over time at 50 ms intervals; re-entry is very stable and maintained by a single rotor. (D) Ratio of depolarized cells and (E) transmembrane potential over time for the cardiomyocyte marked with a white circle in panels A and B.

Figure S11. Representative example of simulated cholinergic AF using pattern #2 with peak ACh concentration of 3.75 nM and the remodeled cardiomyocyte model. (A) ACh distribution with peak concentration of 3.75 nM and (B) corresponding APD_{-60} distribution. (C) Transmembrane potential over time at 50 ms intervals; re-entry is very stable and maintained by a single rotor. (D) Ratio of depolarized cells and (E) transmembrane potential over time for the cardiomyocyte marked with a white circle in panels A and B.

Figure S12. Representative example of simulated cholinergic AF using pattern #3 with peak ACh concentration of 3.75 nM and the remodeled cardiomyocyte model. (A) ACh distribution with peak concentration of 3.75 nM and (B) corresponding APD_{-60} distribution. (C) Transmembrane potential over time at 50 ms intervals; re-entry is stable and maintained by a few rotors. (D) Ratio of depolarized cells and (E) transmembrane potential over time for the cardiomyocyte marked with a white circle in panels A and B.

Figure S13. Representative example of re-entry non-termination by 100% I_{Kur} block using ACh pattern #2 with peak ACh concentration of 3.75 nM and the remodeled cardiomyocyte model. (A) ACh distribution with peak concentration of 3.75 nM and (B) corresponding APD_{-60} distribution. (C) Transmembrane potential over time at 50 ms intervals; 100% I_{Kur} block was introduced at t_{drug} = 1000 ms. (D) Ratio of depolarized cells and (E) transmembrane potential

over time for the cardiomyocyte marked with a white circle in panels A and B for control (blue) and 50% I_{Kur} block (red).

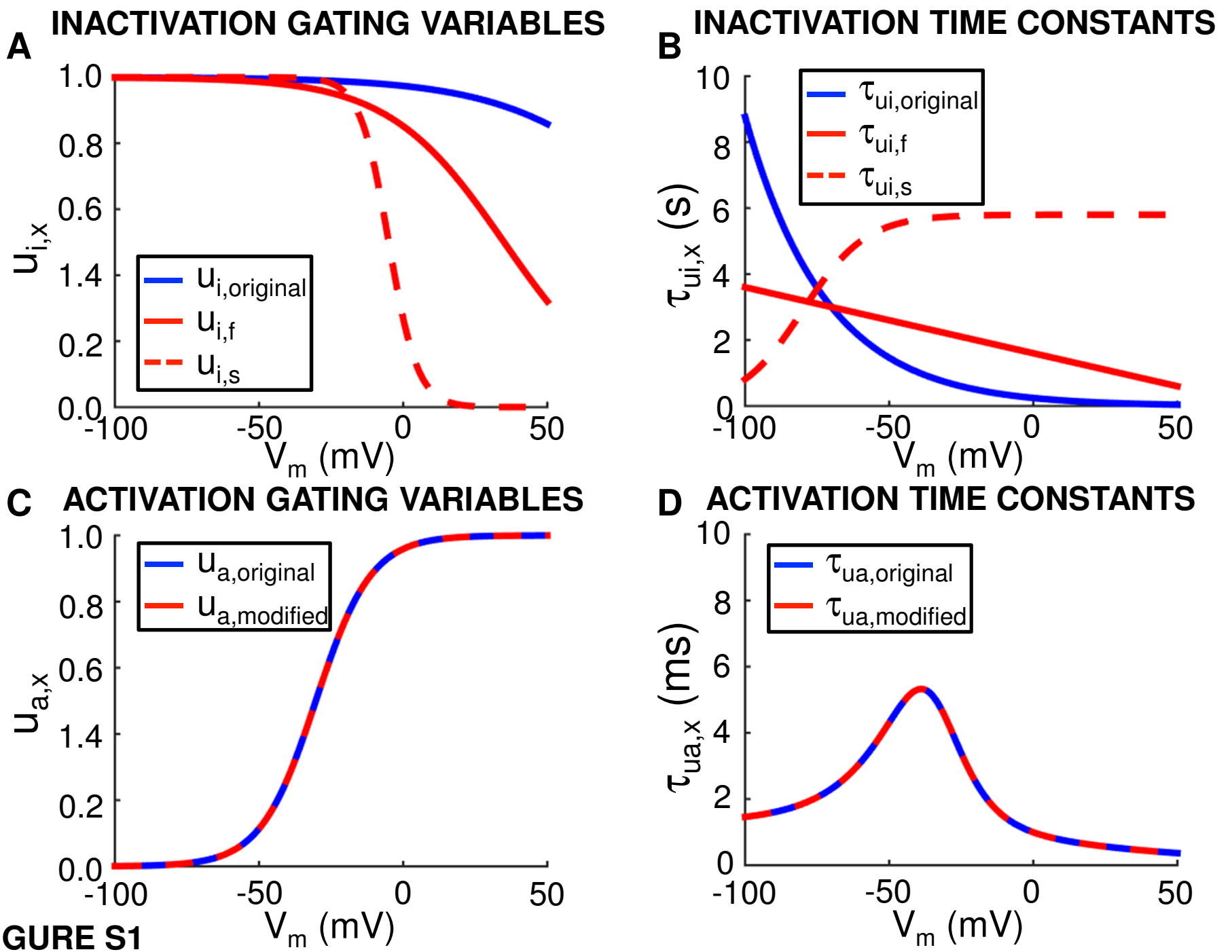
A
INACTIVATION GATING VARIABLES
1.0
0.8
0.6
1.4
0.2
0.0
$u_{i,x}$
$u_{i,original}$
$u_{i,f}$
$u_{i,s}$
-100
-50
0
50
V_m (mV)
B
INACTIVATION TIME CONSTANTS
10
8
6
4
2
0
$\tau_{ui,x}$ (s)
$\tau_{ui,original}$
$\tau_{ui,f}$
$\tau_{ui,s}$
-100
-50
0
50
V_m (mV)
C
ACTIVATION GATING VARIABLES
1.0
0.8
0.6
1.4
0.2
0.0
$u_{a,x}$
$u_{a,original}$
$u_{a,modified}$
-100
-50
0
50
V_m (mV)
D
ACTIVATION TIME CONSTANTS
10
8
6
4
2
0
$\tau_{ua,x}$ (ms)
$\tau_{ua,original}$
$\tau_{ua,modified}$
-100
-50
0
50
V_m (mV)

FIGURE S1

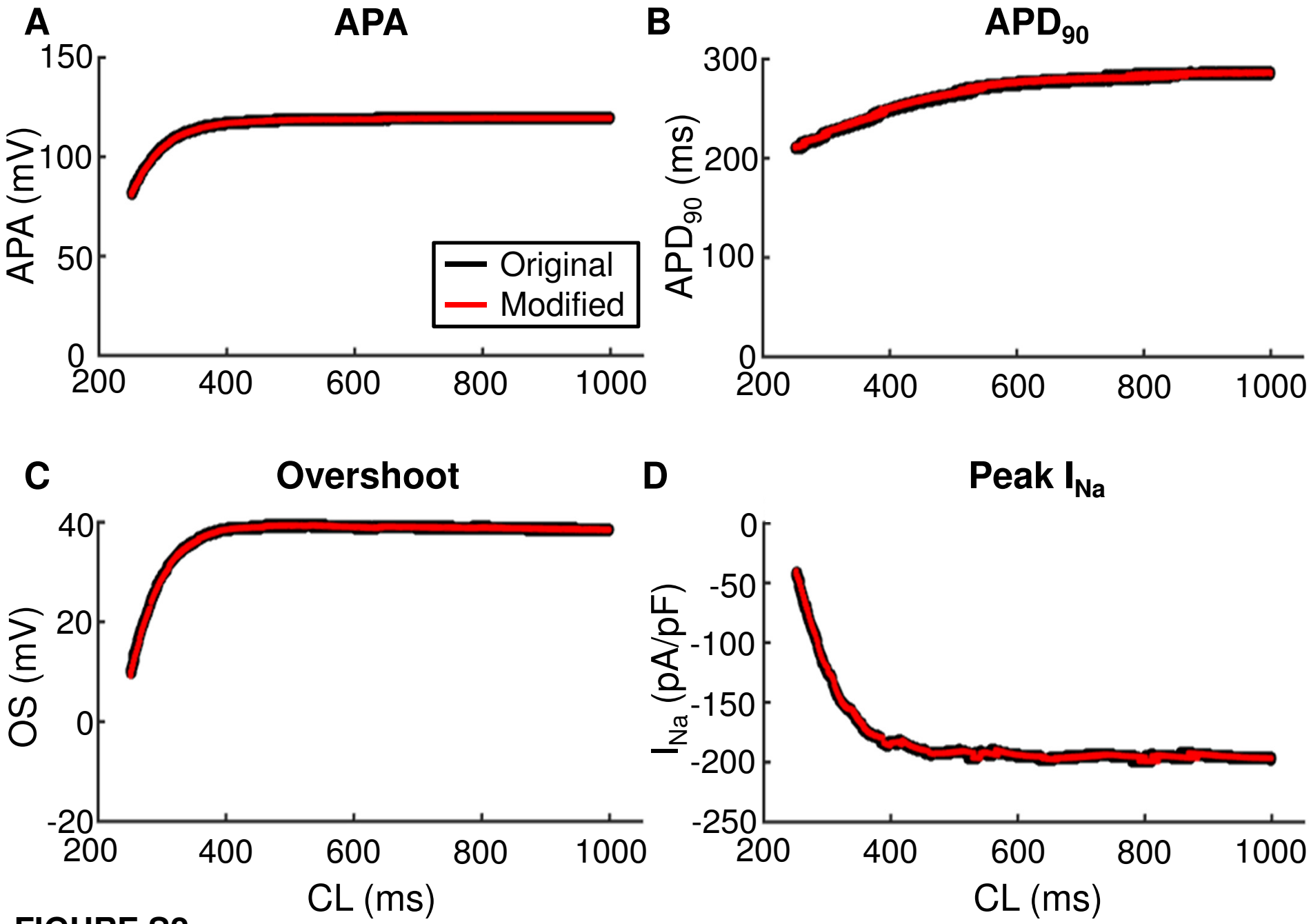
A
APA
APA (mV)
150
100
50
0
200
400
600
800
1000
Original
Modified
B
APD90
APD90 (ms)
300
200
100
0
200
400
600
800
1000
C
Overshoot
OS (mV)
40
20
0
-20
200
400
600
800
1000
CL (ms)
D
Peak INa
INa (pA/pF)
0
-50
-100
-150
-200
-250
200
400
600
800
1000
CL (ms)

FIGURE S2

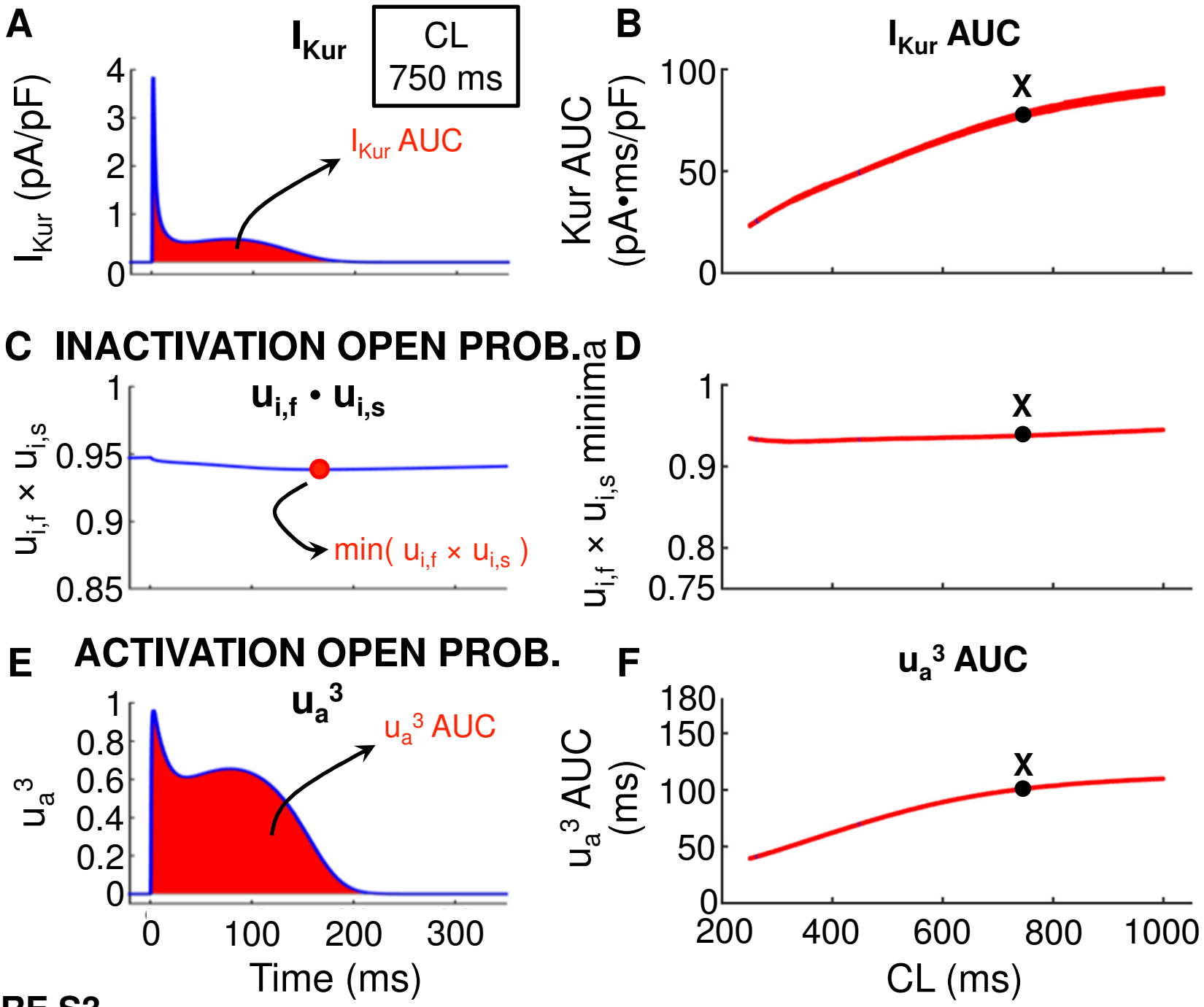
A
I_{Kur}
CL
750 ms
I_{Kur} AUC
I_{Kur} (pA/pF)
4
3
2
1
0
B
I_{Kur} AUC
Kur AUC
(pA•ms/pF)
100
50
0
X
C INACTIVATION OPEN PROB.
$u_{i,f} \bullet u_{i,s}$
$u_{i,f} \times u_{i,s}$
1
0.95
0.9
0.85
min($u_{i,f} \times u_{i,s}$)
D
$u_{i,f} \times u_{i,s}$ minima
1
0.9
0.8
0.75
X
E ACTIVATION OPEN PROB.
u_a^3
u_a^3 AUC
1
0.8
0.6
0.4
0.2
0
0
100
200
300
Time (ms)
F
u_a^3 AUC
u_a^3 AUC (ms)
180
150
100
50
0
X
200
400
600
800
1000
CL (ms)

FIGURE S3

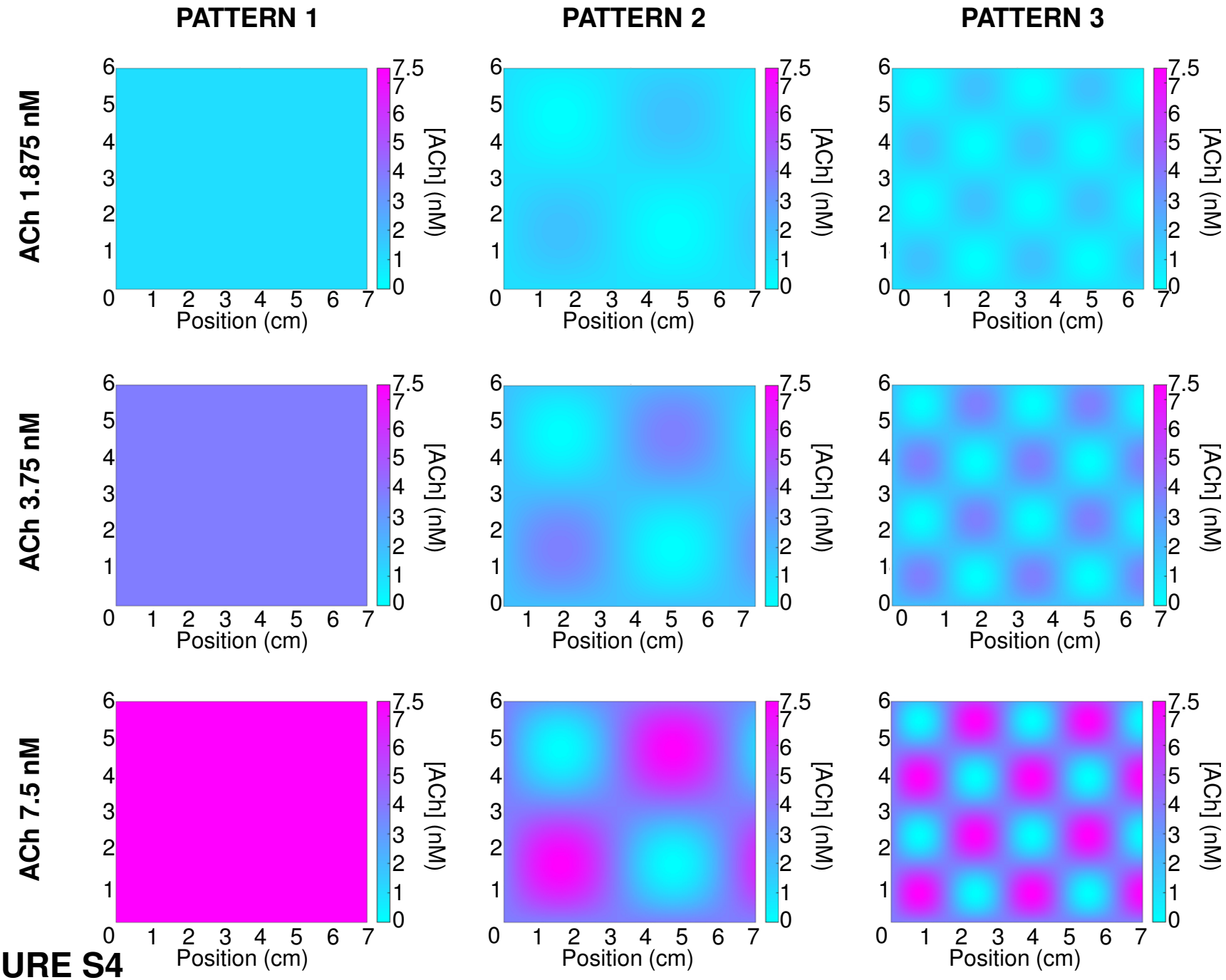
PATTERN 1
PATTERN 2
PATTERN 3
ACh 1.875 nM
ACh 3.75 nM
ACh 7.5 nM
Position (cm)
[ACh] (nM)

FIGURE S4

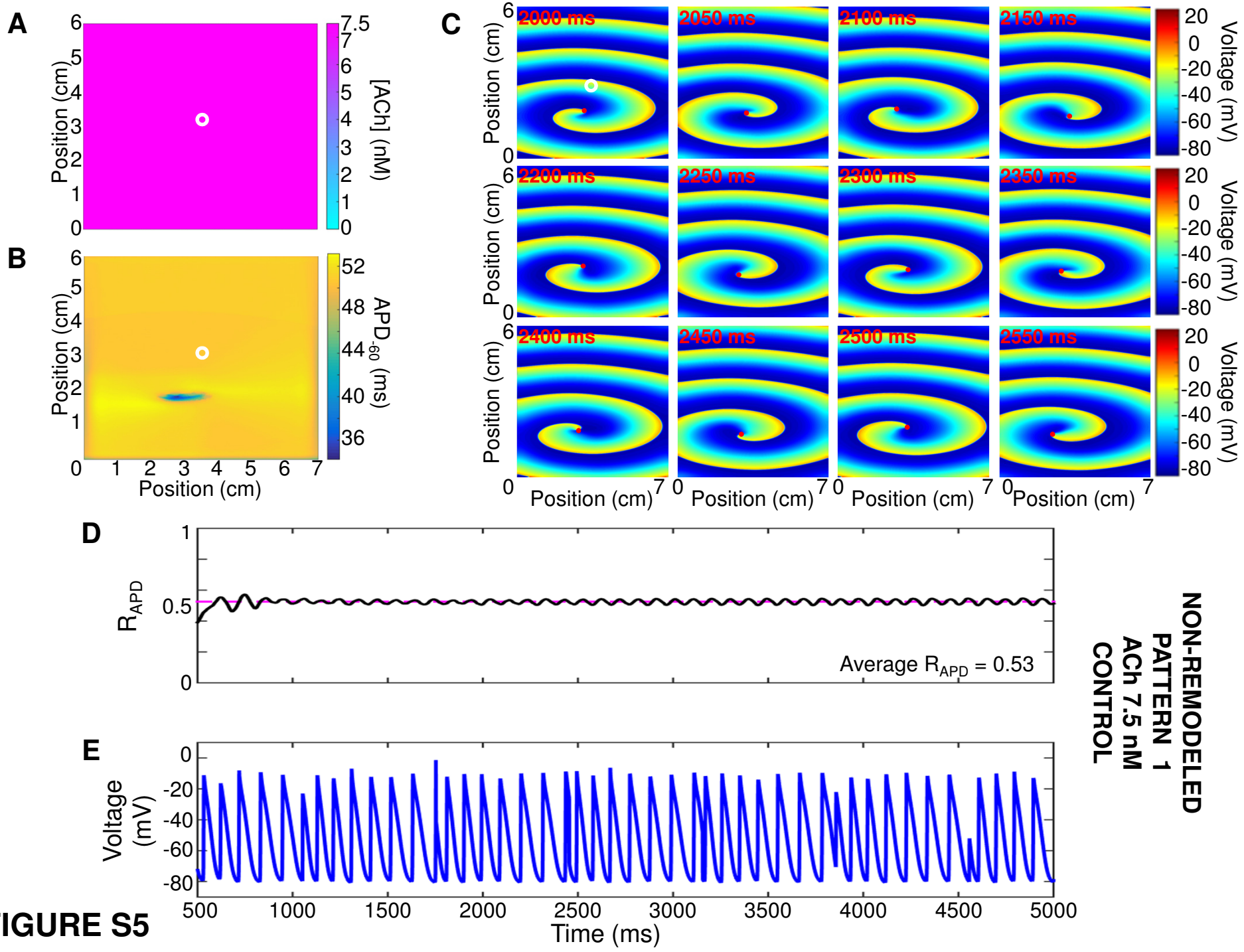
A
B
C
D
E
Position (cm)
[ACh] (nM)
APD90 (ms)
Voltage (mV)
2000 ms
2050 ms
2100 ms
2150 ms
2200 ms
2250 ms
2300 ms
2350 ms
2400 ms
2450 ms
2500 ms
2550 ms
R_APD
Average R_APD = 0.53
Time (ms)
NON-REMODELED
PATTERN 1
ACh 7.5 nM
CONTROL

FIGURE S5

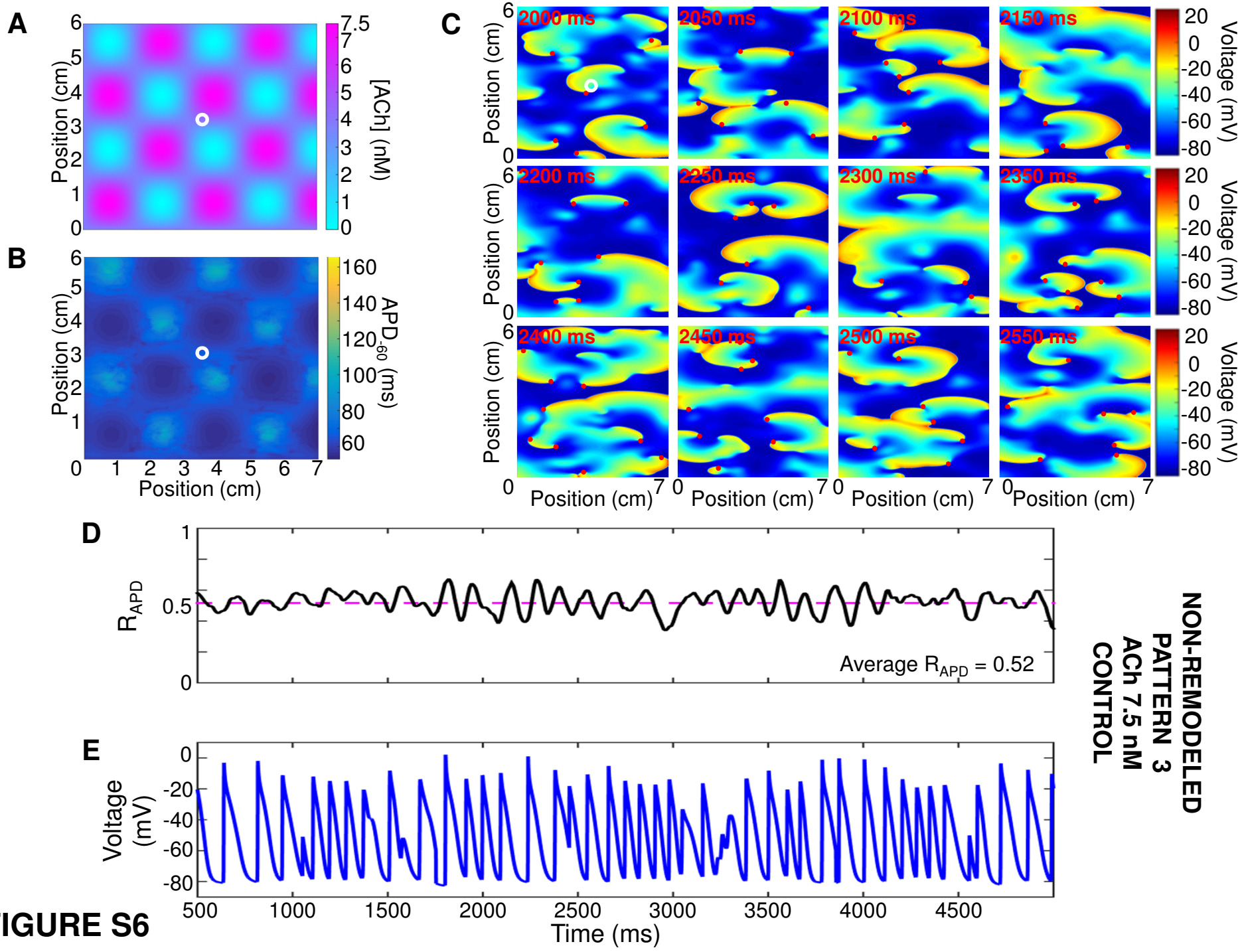
A
B
C
D
E
Position (cm)
[ACh] (nM)
APD90 (ms)
Voltage (mV)
2000 ms
2050 ms
2100 ms
2150 ms
2200 ms
2250 ms
2300 ms
2350 ms
2400 ms
2450 ms
2500 ms
2550 ms
R_APD
Average R_APD = 0.52
Voltage (mV)
Time (ms)
NON-REMODELED
PATTERN 3
ACh 7.5 nM
CONTROL

FIGURE S6

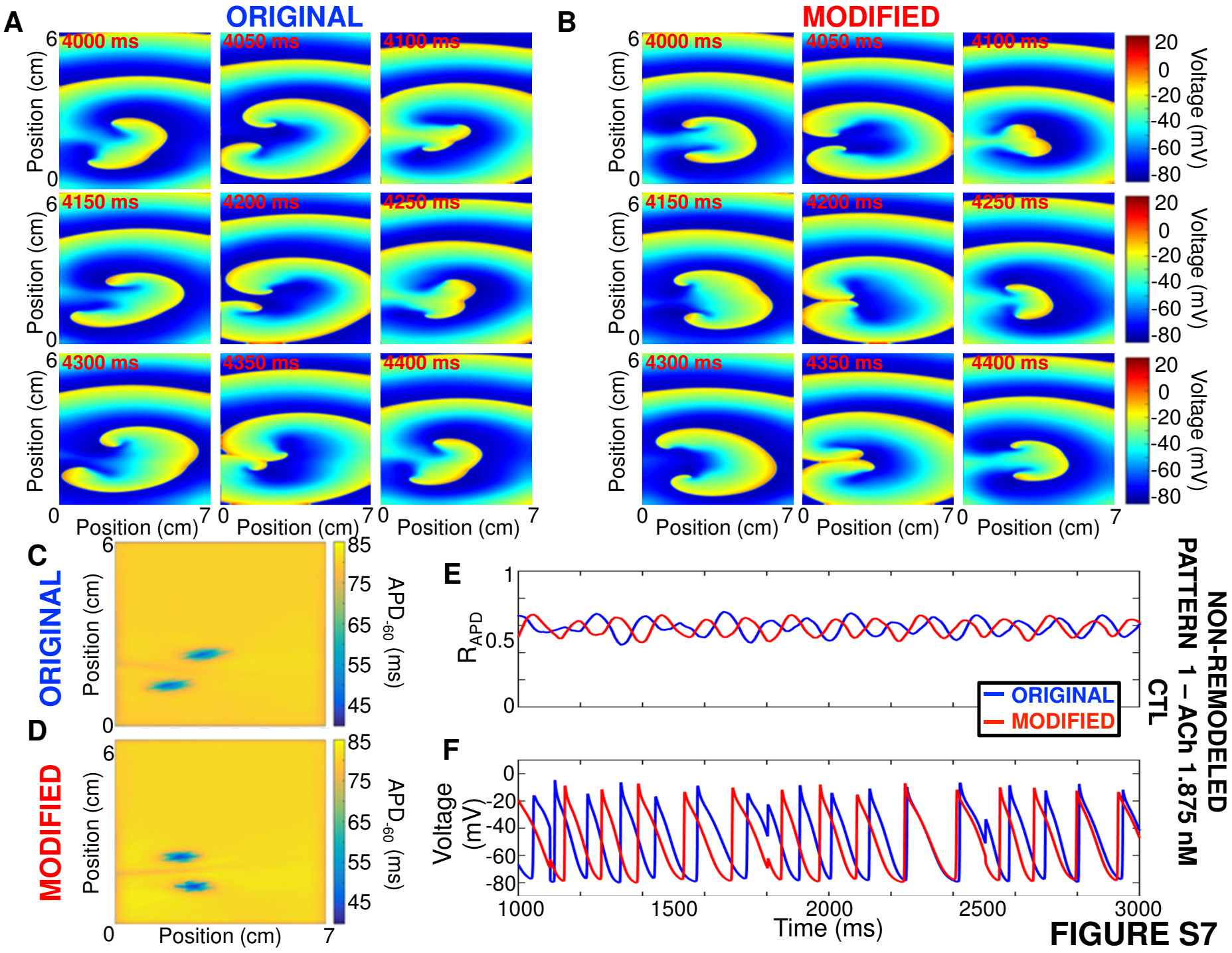
A
ORIGINAL
4000 ms
4050 ms
4100 ms
4150 ms
4200 ms
4250 ms
4300 ms
4350 ms
4400 ms
Position (cm)
B
MODIFIED
Voltage (mV)
C
ORIGINAL
D
MODIFIED
APD-60 (ms)
E
R_APD
ORIGINAL
MODIFIED
F
Voltage (mV)
Time (ms)
NON-REMODELED
PATTERN 1 – ACh 1.875 nM
CTL

FIGURE S7

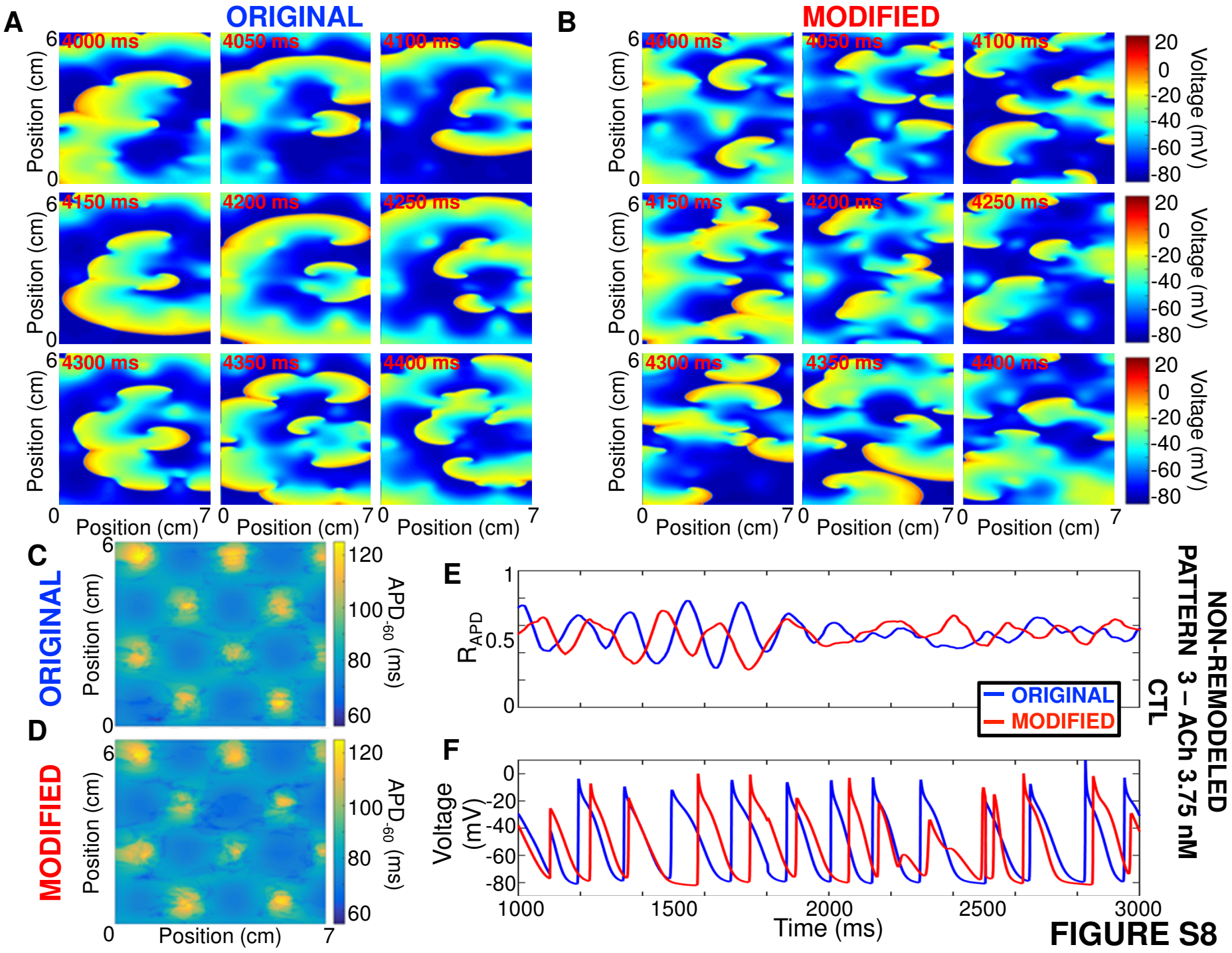
A
ORIGINAL
4000 ms
4050 ms
4100 ms
4150 ms
4200 ms
4250 ms
4300 ms
4350 ms
4400 ms
Position (cm)
B
MODIFIED
Voltage (mV)
C
ORIGINAL
D
MODIFIED
APD-60 (ms)
E
R_APD
ORIGINAL
MODIFIED
F
Voltage (mV)
Time (ms)
NON-REMODELED
PATTERN 3 – ACh 3.75 nM
CTL

FIGURE S8

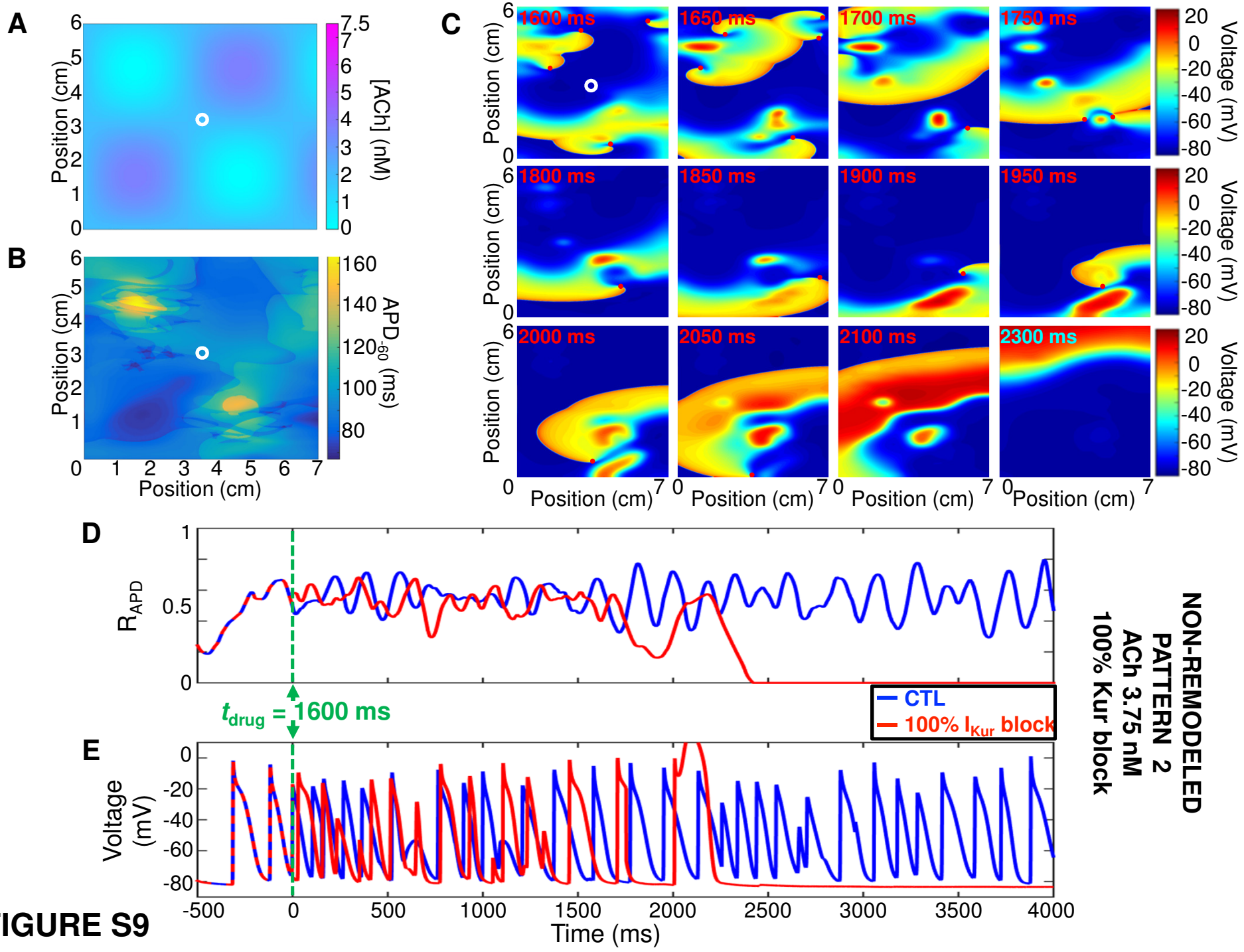
A
B
C
D
E
Position (cm)
[ACh] (nM)
APD90 (ms)
Voltage (mV)
1600 ms
1650 ms
1700 ms
1750 ms
1800 ms
1850 ms
1900 ms
1950 ms
2000 ms
2050 ms
2100 ms
2300 ms
RAPD
tdrug = 1600 ms
CTL
100% IKur block
Voltage (mV)
Time (ms)
NON-REMODELED
PATTERN 2
ACh 3.75 nM
100% Kur block

FIGURE S9

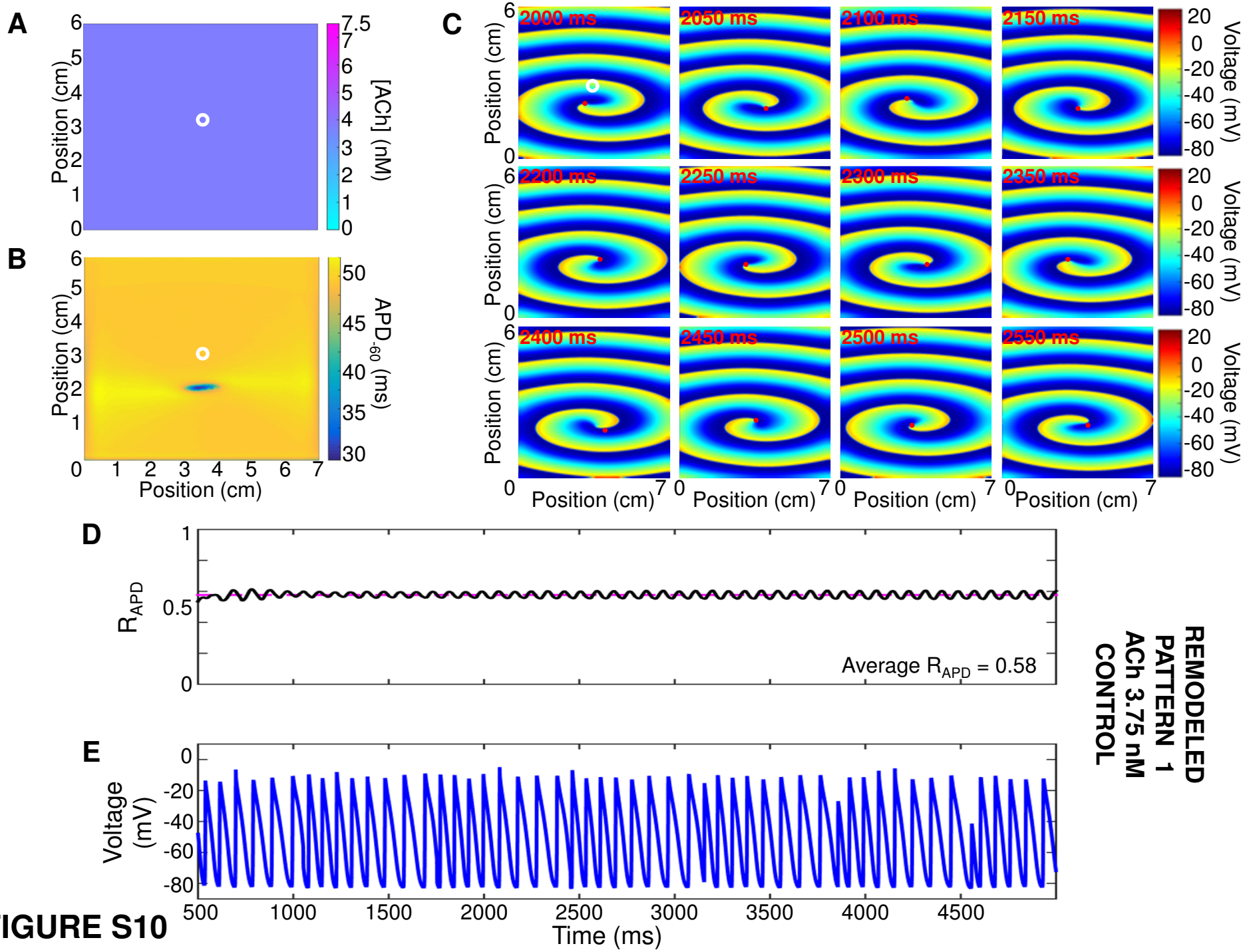
A
B
C
D
E
Position (cm)
[ACh] (nM)
APD90 (ms)
Voltage (mV)
2000 ms
2050 ms
2100 ms
2150 ms
2200 ms
2250 ms
2300 ms
2350 ms
2400 ms
2450 ms
2500 ms
2550 ms
R_APD
Average R_APD = 0.58
Time (ms)
REMODELED
PATTERN 1
ACh 3.75 nM
CONTROL

FIGURE S10

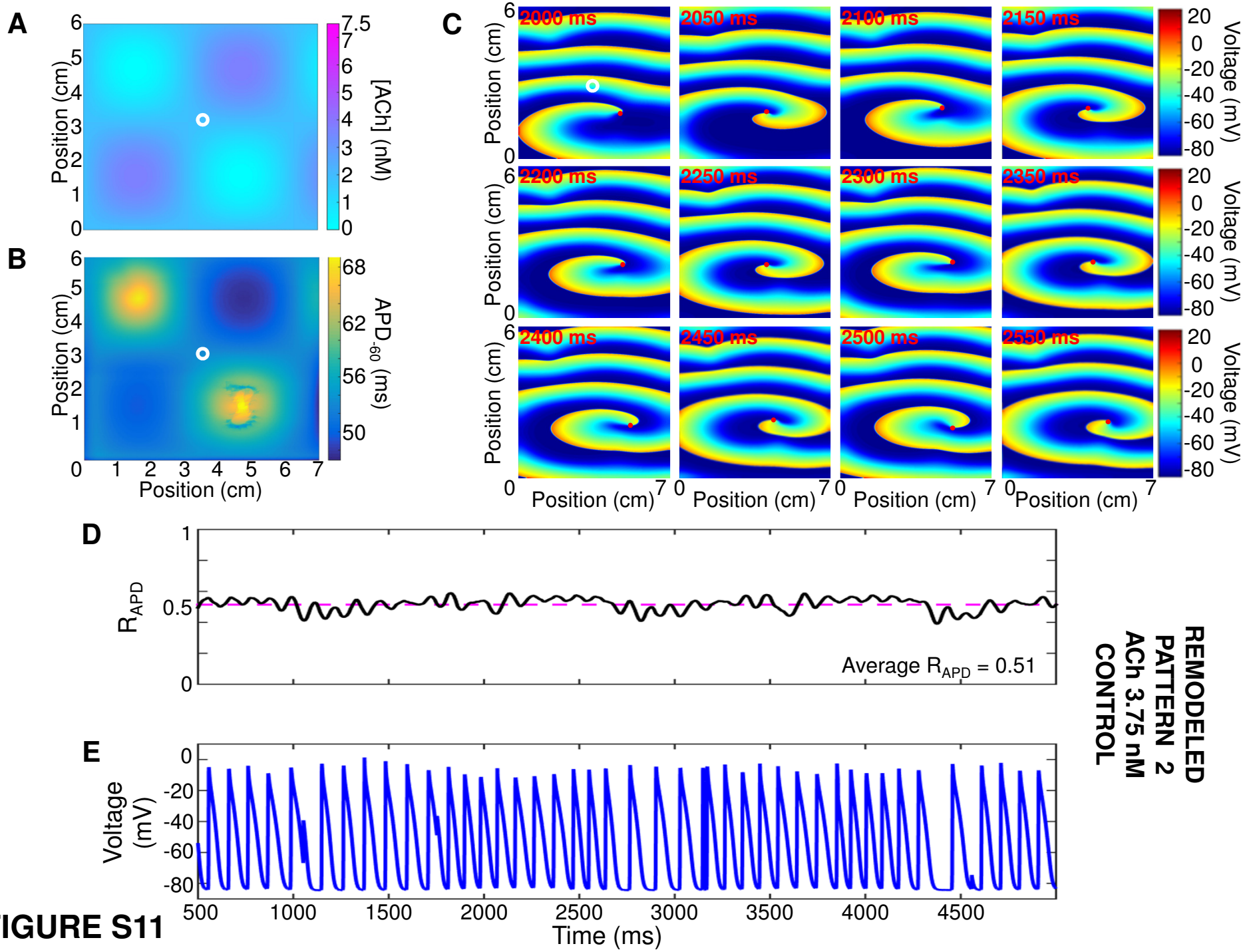
A
B
C
D
E
Position (cm)
[ACh] (nM)
APD90 (ms)
2000 ms
2050 ms
2100 ms
2150 ms
2200 ms
2250 ms
2300 ms
2350 ms
2400 ms
2450 ms
2500 ms
2550 ms
Voltage (mV)
R_APD
Average R_APD = 0.51
Voltage (mV)
Time (ms)
REMODELED
PATTERN 2
ACh 3.75 nM
CONTROL

FIGURE S11

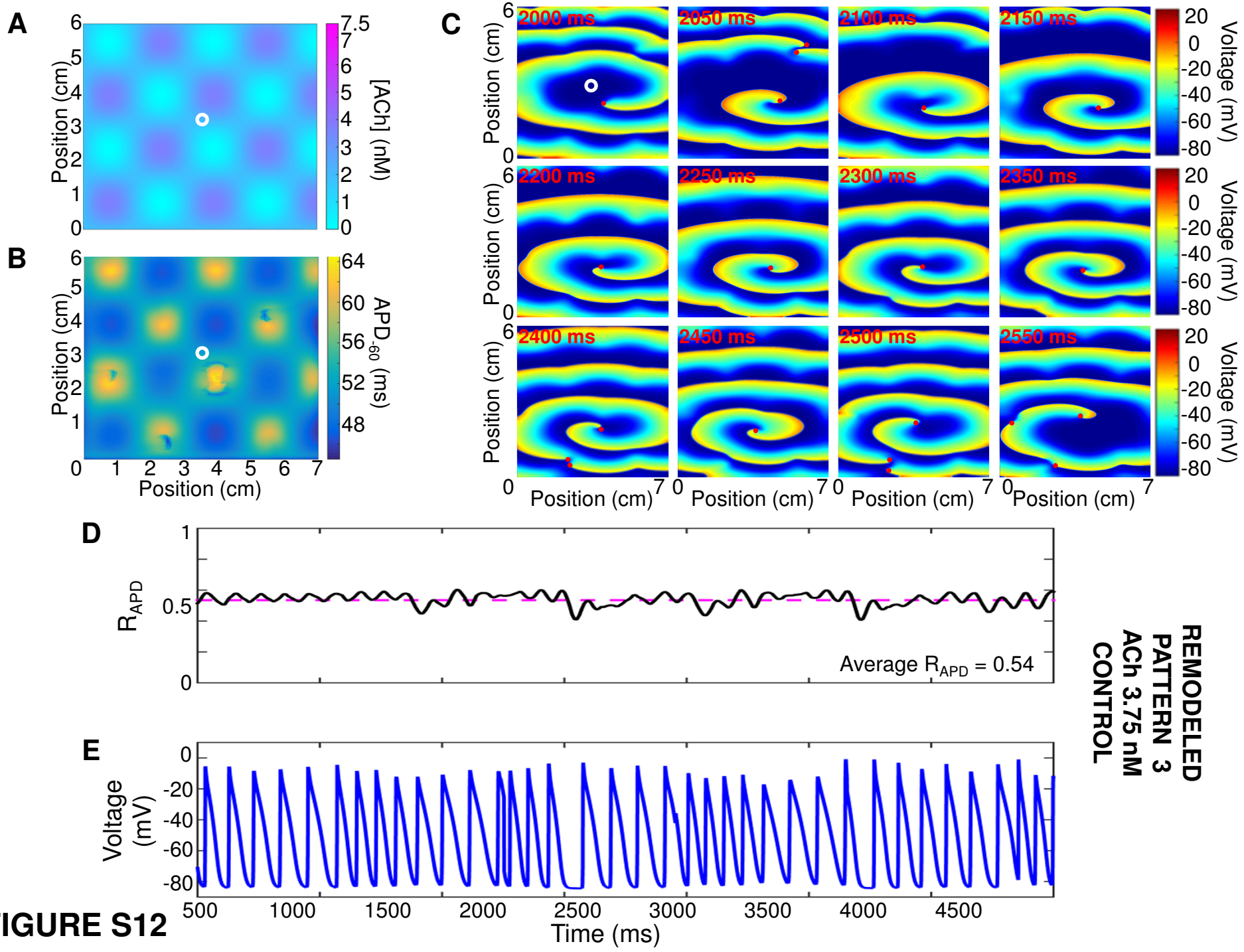
A
B
C
D
E
Position (cm)
[ACh] (nM)
APD90 (ms)
2000 ms
2050 ms
2100 ms
2150 ms
2200 ms
2250 ms
2300 ms
2350 ms
2400 ms
2450 ms
2500 ms
2550 ms
Voltage (mV)
R_APD
Average R_APD = 0.54
Voltage (mV)
Time (ms)
REMODELED
PATTERN 3
ACh 3.75 nM
CONTROL

FIGURE S12

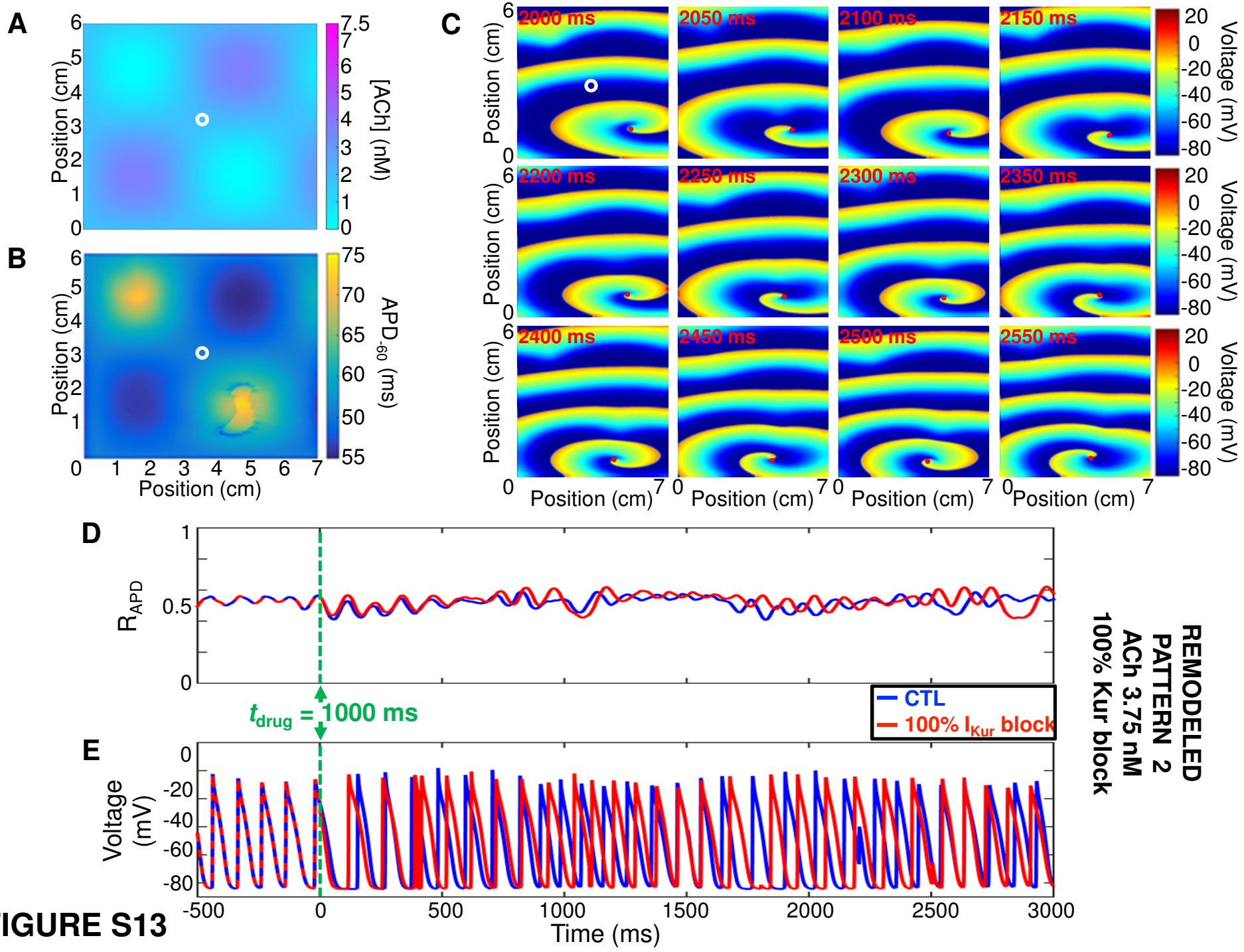
A
B
C
D
E
Position (cm)
[ACh] (nM)
APD90 (ms)
Voltage (mV)
2000 ms
2050 ms
2100 ms
2150 ms
2200 ms
2250 ms
2300 ms
2350 ms
2400 ms
2450 ms
2500 ms
2550 ms
RAPD
tdrug = 1000 ms
CTL
100% IKur block
Time (ms)
REMODELED
PATTERN 2
ACh 3.75 nM
100% Kur block

FIGURE S13